How well are aerosol-cloud interactions represented in climate models? Part 1: Understanding the sulphate aerosol production from the 2014-15 Holuhraun eruption.

George Jordan[1], Jim Haywood[1,2], Florent Malavelle[3], Ying Chen[4], Amy Peace[2], Eliza Duncan[2], Daniel G. Partridge[2], Paul Kim[2], Duncan Watson-Parris[5], Toshihiko Takemura[6], David Neubauer[7], Gunnar Myhre[8], Ragnhild Skeie[8] and Anton Laakso[9]

[1] Met Office Hadley Centre, Exeter, UK
[2] College of Engineering, Mathematics, and Physical Sciences, University of Exeter, Exeter, UK
[3] Met Office, Exeter, UK
[4] School of Geography Earth and Environment Sciences, University of Birmingham, UK~~Laboratory of Atmospheric Chemistry, Paul Scherrer Institute, Switzerland~~
[5] Scripps Institution of Oceanography and Halicioğlu Data Science Institute, University of California San Diego, La Jolla, CA, USA
[6] Kyushu University, Fukuoka, Japan
[7] Institute for Climate and Atmospheric Science, ETH Zurich, Zurich, Switzerland
[8] CICERO Center for International Climate and Environmental Research, Oslo, Norway
[9] Finnish Meteorological Institute, Atmospheric Research Centre of Eastern Finland, Kuopio, Finland

Correspondence to: George Jordan (george.jordan@metoffice.gov.uk)

Abstract. For over 6-months, the 2014–2015 effusive eruption at Holuhraun, Iceland injected considerable amounts of sulphur dioxide (SO_2) into the lower troposphere with a daily rate of up to one-third of the global emission rate causing extensive air pollution across Europe. The large injection of SO_2, which oxidises to form sulphate aerosol (SO_4^{2-}), provides a natural experiment offering an ideal opportunity to scrutinise state-of-the-art general circulation models' (GCMs) representation of aerosol-cloud interactions (ACIs). Here we present Part 1 of a two-part model inter-comparison using the Holuhraun eruption as a framework to analyse ACIs. We use SO_2 retrievals from the Infrared Atmospheric Sounding Interferometer (IASI) instrument and ground-based measurements of SO_2 and SO_4^{2-} mass concentrations across Europe in conjunction with a trajectory analysis using the Hybrid Single Particle Lagrangian Integrated Trajectory (HYSPLIT) model to assess the spatial and chemical evolution of the volcanic plume as simulated by 5 GCMs and a chemical transport model (CTM). IASI retrievals of plume altitude and SO_2 column load reveal that the volcanic perturbation is largely contained within the lower troposphere. Compared to the satellite observations, the models capture ~~and that~~ the spatial evolution and vertical variability of the plume ~~is~~ reasonably well ~~captured by the models~~, although ~~the~~ the ~~the~~ models often ove~~unde~~restimate the ~~mean~~ plume altitude. HYSPLIT trajectories are used to attribute to Holuhraun emissions 1118~~4~~ instances of elevated sulphurous surface mass concentrations recorded at European Monitoring and Evaluation Programme (~~22 air monitoring~~ EMEP) stations across Europe during September and October 2014. Comparisons with the simulated concentrations show that ~~the~~ the ratio of SO_2-to-SO_4^{2-} during these pollution episodes ~~models underestimate the elevated SO_2 concentrations observed at stations closer to Holuhraun whilst~~

~~overestimating those observed further away.~~ is often underestimated and overestimated for the young and mature plume respectively. Models with finer vertical resolutions near the surface are found to better capture these elevated sulphurous ground-level concentrations. Using an ~~bi~~exponential function to describe the decay of observed surface mass concentration ratios of SO_2-to-SO_4^{2-} with plume age, the in-plume oxidation rate constant ~~gas-phi~~as ~~e and aqueous-phase oxidation rates are~~ estimated as 0.03~~21~~ ± 0.002 h^{-1} (1.30 ± 0.08 day *e*-folding time) ~~and 0.22 ± 0.16 h^{-1} respectively~~ with a near-vent ratio of 25~~31~~ ± ~~5~~4 [µgm^{-3} of SO_2 / µgm^{-3} of SO_4^{2-}]. The majority of the corresponding derived modelled ~~gas-phase~~ oxidation rate constants ~~from the models~~ are ~~all~~ lower than the observed estimate. ~~, whilst the majority of the aqueous-phase oxidation rates agree with the observed rate.~~ This suggests that the representation of the ~~simulated~~oxidation pathway/s in the simulated plumes is too slow~~capture the observed chemical behaviour in the young plume (when aqueous-phase oxidation is dominant), yet not in the mature plume (when gas-phase oxidation is dominant)~~. Overall, despite their coarse spatial resolutions, the 6 models show reasonable skill in capturing the spatial and chemical evolution of the Holuhraun plume. This capable representation of the underlying aerosol perturbation is ~~which is~~ essential to enable the investigation of ~~when exploring~~ the eruption's impact on ACIs in the second part of this study.

Formatted: Font color: Auto

1 Introduction

The Bárðarbunga volcanic system in Iceland began experiencing noteworthy sequences of earthquakes on 16th August 2014 (Ágústsdóttir et al., 2016; Gudmundsson et al., 2014; Sigmundsson et al., 2015). This seismic activity created an effusive eruption at Holuhraun (64.85°N, 16.83°W) from 31st August 2014 to 27th February 2015. The resulting flow of lava is estimated to have covered 84 km^2 with an average discharge rate of 90 m^3s^{-1} making it the largest effusive eruption in Iceland since the 1783-1784 Laki eruption (Pedersen et al., 2017). Ground-based observation estimates suggest the Holuhraun eruption released a total of 9.6–11.8 Mt of sulphur dioxide (SO_2) with little tephra (Gíslason et al., 2015; Pfeffer et al., ~~2019~~2018). These emissions represent up to 215 times the amount of Icelandic anthropogenic SO_2 emissions for 2019 (Keller et al., 2022) and approximately one tenth of the current global annual anthropogenic emissions (e.g. Aas et al., 201~~9~~5). During these months of intense degassing, several studies using ground-based observations and remote sensing suggest that the volcanic plume reached altitudes of 1–4 km (Arason et al., 2015; Carboni et al., 2019a; Flower and Kahn, 2020; Pfeffer et al., ~~2019~~2018). This release of SO_2 adversely affected air quality over large parts of Iceland often exceeding World Health Organization (WHO) surface concentration limits (Gíslason et al., 2015; Ilyinskaya et al., 2017; Schmidt et al., 2015). Such high rates of SO_2 emission into a relatively pristine, unpolluted environment provide an ideal opportunity to observe ~~aerosol~~ aerosol-cloud interactions (ACIs~~)~~ ~~(e.g. Breen et al., 2021; Chen et al., 2022; Gettelman et al., 2015; Haghighatnasab et al., 2022; Malavelle et al., 2017, McCoy and Hartmann, 2015, Toll et al., 2017))~~ and elucidate aerosol impacts on the climate system~~)~~ (e.g. Breen et al., 2021; Chen et al., 2022; Gettelman et al., 2015; Haghighatnasab et al., 2022; Malavelle et al., 2017, McCoy and Hartmann, 2015, Toll et al., 2017).

Remote sensing data estimates of SO_2 concentrations, a common tool to monitor the evolution of volcanic plumes, show that the September and October meteorological conditions transported the plume across Europe including the Fennoscandian Peninsula (Grahn et al., 2015; Ialongo et al., 2015), Belgium, northern France (Boichu et al., 2016), the UK, Ireland, the Netherlands (Schmidt et al., 2015) and Germany (Steensen et al., 2016). Previous studies have combined satellite data with ground-based observations and trajectory modelling to attribute local pollution events to the Holuhraun eruption and investigate the plume characteristics (e.g. Boichu et al., 2019; Schmidt et al., 2015; Twigg et al., 2016). Understanding such characteristics, particularly those that are hazardous to health (i.e. ~~such as~~ fine particulate matter), is important for air quality monitoring and attribution of any exceedances of statutory thresholds (Heaviside et al. 2021; Stewart et al., 2022). However, most studies ~~that assessed~~assessing Holuhraun impacts on air quality focus only on ~~the~~ pollution experienced at a few ground-based stations across small geographical areas and the need to ~~expand~~ increase the quantity of air monitoring stations ~~used~~ investigated has been noted previously (Schmidt et al., 2015; Twigg et al., 2016).

In addition to ~~the~~ observational evidence, many studies have explored the impacts of the Holuhraun eruption using ~~also used~~ numerical mode~~lls~~ling to simulate the transport of the volcanic SO_2 ~~emitted by the Holuhraun eruption~~emissions. For instance, the Icelandic Meteorological Office employed the CALPUFF dispersion model for near-time probabilistic hazard mapping (Barsotti, 2020) and to support aviation safety decisions (Barsotti et al., 2020) following the eruption. ~~Furthermore,~~ Boichu et al. (2016) and Steensen et al. (2016) used the EMEP MSC-W and the CHIMERE chemical transport models (CTMs) respectively to explore the far-range air pollution effects caused by the eruption, whereas Schmidt et al. (2015) used the NAME dispersion model to do so. Recently, Haghighatnasab et al. (2022) analysed the results from high resolution simulations performed with the ICON model in its numerical weather prediction mode to explore the impact of the aerosol perturbation~~s~~ introduced by Holuhraun on cloud properties. This impact was also examined in earlier works using general circulation models (GCMs) of coarser resolutions (CAM5 – Gettelman et al., 2015; HadGEM3, CAM5, and a NorESM variant – Malavelle et al., 2017). Considering the opportunity the Holuhraun eruption presents to assess the modelling capability of GCMs in capturing aerosol-cloud interactions, the number of GCM studies of the Holuhraun eruption to date is surprisingly low.

Here we present results from an inter-model comparison two-part study of the volcanic plume and its interactions with clouds within the vicinity of the Holuhraun eruption (44°N to 80°N, 60°W to 30°E) during September and October 2014. Participation in the study was organised through the AeroCom initiative (Schulz et al., 2006). We begin with a comparison of the volcanic SO_2 plume evolution between remote sensing observations and simulations of the eruption from 5 GCMs and a CTM. The analysis specifically focuses on the plume spatial distribution, plume altitude, and the total SO_2 mass burden. We further investigate the numerical models' capability to simulate the Holuhraun eruption by comparing modelled SO_2 and sulphate (SO_4^{2-}) concentrations with in situ surface observations from 25 long-term monitoring stations from the European Monitoring and Evaluation Programme (EMEP ~~(European Monitoring and Evaluation Programme~~) network. By using remote sensing and ground-based observations in conjunction with trajectory modelling, we ~~can~~ attribute sulphurous pollution events ~~dominated~~

by sulphur to the Holuhraun emissions and assess the skillss of the different numerical models in capturing these episodevents. Finally, this refined catalogue of volcanically influenced pollution events is used to estimate the rate at which SO_2 oxidises to SO_4^{2-} within both observed and modelled volcanic plumes. We conclude with a discussion of whether the models simulate the observed Holuhraun aerosol perturbation with sufficient fidelity; a prerequisite for understanding the climatic impacts of the Holuhraun caused by the eruption via ACIs (see Part 2 of this study).

2 Methodology

We provide a brief description of the remote sensing and in situ observations that are used to assess the numerical models, the numerical models themselves, and the HYSPLIT trajectory modelling framework used to evaluate the pollutant transport ~~estimate the origin and age of~~of the observed local sulphurous ~~pollution~~ events.

2.1 Satellite Observations

Retrievals of volcanic SO_2 from satellite instrumentation typically use either measurements in the ultra-violet (e.g. Ozone Mapping and Profiler Suite – Nadir Mapper (OMPS-NM); Carn et al., 2015; Li et al., 2017; Wells et al., 2023; TROPOspheric Monitoring Instrument (TROPOMI); de Leeuw et al., 2021; Theys et al., 2017; Global Ozone Monitoring Experiment-2 (GOME-2); Twigg et al., 2016) or infra-red (e.g. Infrared Atmospheric Sounding Interferometer (IASI); Clarisse et al., 2008, 2010, Haywood et al., 2010, de Leeuw et al., 2021) region of the electromagnetic spectrum. Here we use IASI measurements as they have proved valuable in monitoring the evolution of volcanic plumes in both the stratosphere (e.g. Haywood et al., 2010; de Leeuw et al., 2021) and the troposphere (e.g. Athanassiadou et al., 2016; Malavelle et al., 2017). Specifically, we use data from IASI retrievals on the MetOp-A and MetOp-B satellites produced by the University of Oxford as part of the NERC Centre for the Observation and Modelling of Earthquakes, Volcanoes and Tectonics (COMET) (Carboni et al., 2019a, b).

SO_2 column load and plume height are~~is~~ derived by applying the IASI retrieval algorithm of Carboni et al. (2012, 2016) to level 1C data from the EUMETSAT and CEDA archive. The IASI SO_2 retrieval is performed only on pixels where the underlying SO_2 detection scheme returns a ~~is~~ positive result. The detection scheme is a linear retrieval where a positive result is defined as when the free parameter, the SO_2 column load, exceeds a defined threshold. This threshold is set substantially greater than the standard deviation of the assumed Gaussian distribution describing the background atmospheric concentration of SO_2. Consequently, a positive result is exceedingly likely to be significantly different to the background, and not a consequence of instrumental noise or climatological variations (~~which in this scheme is explicitly defined as where the SO_2 column load > 0.49 Dobson units (DU). This detection threshold is based on the significance of a value in relation to the climatology whilst also accounting for the total retrieval error~~ (see details in Walker et al. 2011, 2012). The threshold defined for the Holuhraun eruption in Carboni et al. (2019a) is 0.49 effective DU.

An iterative optimal estimation~~The~~ retrieval using forward modelled spectra ~~algorithm~~ is applied to ~~these detected~~ pixels with a positive detection result. This retrieval uses all channels within 1000–1200 cm^{-1} and 1300–1410 cm^{-1} (the 7.3 μm and 8.7 μm SO_2 bands respectively) and assumes a Gaussian vertical SO_2 profile to return the SO_2 column load (DU) and height (mb) which the retrieval algorithm~~is~~ subsequently convert~~ed~~ to km using European Centre for Medium-Range Weather Forecasts (ECMWF) meteorological ~~temperature~~ profiles. The algorithm provides a comprehensive pixel-by-pixel error estimate on the retrieved parameters that is derived from an error covariance matrix computed using the differences between the measured

Formatted: Subscript

Formatted: Subscript

IASI spectra and the simulated spectra (driven by ECMWF data). This means uncertainty due to imperfect knowledge of non-SO_2 atmospheric conditions (e.g. cloudiness, vertical distribution of constituents) and imperfect radiative transfer simulations are addressed (see details in Carboni et al., 2012). The thermal contrast between the plume and surface heavily influences the retrievalis error such that retrievals of SO_2 plumes centred at lower altitudes have higher uncertainties. This study groups the individual IASI orbits into bidaily intervals (AM: 00:00–12:00 UTC, PM: 12:00–24:00 UTC). Note that the IASI retrieval algorithm can miss parts of the SO_2 plume, such as when overlaying clouds are present or under conditions of negative thermal contrast, and so the IASI SO_2 column loads and mass burdens presented here should be considered an approximate minimum.

This study maps Ddata from individual IASI overpasses to a regular 1.0° x 1.0° latitude-longitude grid using a each group of orbits are resampled to a regular 0.125° x 0.125° grid using a nearest neighbours with Gaussian weighting approach with overlapping values averaged. The decision to weight closer neighbouring pixels allows retention of plume characteristics which can change abruptly over small spatial scales. The individual gridded overpass data are grouped into bidaily intervals (AM: 03:30–15:30, PM: 15:30–03:30) with overlapping cells averaged. Linear interpolation is used to estimate missing values in the gridded output that result from orbital gaps and/or pixels failing quality control. Primarily the SO_2 retrievals from MetOp-A orbits are used, yet when coverage is sparse, those from MetOp-B are also used. Each bidaily regridded IASI SO_2 column load and altitude maps are is visually inspected to ensure no obvious artefacts exist within the Holuhraun vicinity. Note that the IASI retrieval algorithm can miss parts of the SO_2 plume, such as when overlaying clouds are present or under conditions of negative thermal contrast, and so the IASI SO_2 column loads and burdens presented here should be considered to be an approximate minimum.

Formatted: Subscript

Formatted: Pattern: Clear (Yellow)

2.2 Surface Observations

Since the early 1970s, the EMEP network has monitored air pollution and surface deposition across Europe at surface ground-level stations outside of notablesignificant conurbations where significant sources of l that are only weakly affected by local pollution are minimised thus creating a comprehensive database useful for assessing long-range transportation of a plethora of pollutants (Tørseth et al., 2012). The use of EMEP stations to evaluate model output has proven fruitful previously (e.g. Hardacre et al., 2021; Mulcahy et al., 2020). This study only considers EMEP stations that provide both SO_2 and SO_4^{2-} surface mass concentration measurements at the same temporal sampling frequency during September and October 2014. This criterion results. inThe 25 EMEP stations located across 12 countries being selected for this study (see are listed in Table 1). The observations include hourly and daily measurements made using online ion chromatography and filter-pack measurements respectively, with the former to a precision of 0.001 μgm^{-3} and the latter to either 0.01 μgm^{-3} or 0.001 μgm^{-3} depending on the station. The hourly and daily sampling midpoints are centred on 30 minutes past the hour and on the hour respectively. Further details on the instruments and sampling techniques are provided in the EMEP Standard Operating Protocol (NILU, 2014). This study screens out invalid and missing measurements in accordance with the EMEP data quality flags (NILU, 2020). For each

station monthly surface mass concentration climatologies for SO_2, and SO_4^{2-} are calculated from the temporal coverage listed in Table 1. For a given station this coverage may differ for the two chemical species. Subsequently, the combined total sulphur content climatologies are only calculated across periods where the temporal coverages align (e.g. 1988–2017 for Aspvreten and 2006–2020 for Irafoss). and combined total sulphur are calculated from the full temporal coverage available and used to assess significance. Here we define a significant sulphurous pollution event is defined as when the surface mass concentration of the total sulphur content observed exceeds the 90th percentile of the corresponding monthly climatological value. Note that the number of EMEP stations carrying out SO_2 and SO_4^{2-} measurements has fallen since the late 2000s due to the reduced need to monitor the declining sulphur emissions from anthropogenic sources (Boichu et al., 2019; Schmidt et al., 2015). The 25 EMEP stations located across 12 countries selected for this study are listed in Table 1.

Table 1: Details of the 25 EMEP stations explored in this study. These stations are shown geographically in Fig. 1.

Station name (EMEP code)	**Country**	**Sampling details**			**Coordinates**		**Trajectory details**	
		Instrument type/s	**Frequency**	**Temporal coverage**	**Lat. lon. (°N, °E)**	**Alt. (m AMSL)**	**Starting height (m AGL)**	**Bounding radius (km)**
Anholt (DK0008R)	Denmark	Filter-3pack	Daily	1989-2020	(56.72°, 11.52°)	40	100	380
Aspvreten (SE0012R)	Sweden	Filter-3pack Filter-2pack Filter-1pack	Daily	1984-2017 (SO_2 from 1988)	(58.80°, 17.38°)	20	100	440
Auchencorth Moss (GB0048R)	Scotland	Online Ion Chroma.	Hourly	2007-2020	(55.79°, -3.24°)	260	250	320
Birkenes II (NO0002R)	Norway	Filter-3pack	Daily	2010-2020	(58.39°, 8.25°)	219	100	320
Bredkälen (SE0005R)	Sweden	Filter-3pack Filter-2pack Filter-1pack	Daily	1980-2020 (SO_2 from 1992)	(63.85°, 15.33°)	404	100	380
Harwell (GB0036R)	England	Online Ion Chroma.	Hourly	2009-2015 (SO_2 from 2011)	(51.57°, -1.32°)	137	100	380
Hurdal (NO0056R)	Norway	Filter-3pack	Daily	1997-2020	(60.37°, 11.08°)	300	100	320
Irafoss (IS0002R)	Iceland	Filter-2pack Filter-1pack	Daily	1980-2020 (SO_2 from 2006)	(64.08°, -21.02°)	66	100	72
Kårvatn (NO0039R)	Norway	Filter-3pack Filter-2pack	Daily	1980-2020	(62.78°, 8.88°)	210	100	320
Leba (PL0004R)	Poland	Filter-2pack Filter-1pack	Daily	1993-2020	(54.75°, 17.53°)	2	100	500
Neuglobsow (DE0007R)	Germany	Filter-3pack Filter-1pack	Daily	1981-2018 (SO_2 from 2000)	(53.17°, 13.03°)	62	100	500
Pallas Matorova (FI0036R)	Finland	Filter-3pack Filter-2pack	Daily	1996-2020	(68.00°, 24.24°)	340	250	440
Preila (LT0015R)	Lithuania	Filter-3pack Filter-2pack	Daily	1991-2020 (SO_2 from 1996)	(55.38°, 21.03°)	5	250	500
Råö (SE0014R)	Sweden	Filter-3pack	Daily	2002-2020	(57.39°, 11.91°)	5	100	380
Risoe	Denmark	Filter-3pack	Daily	2011-2020	(55.69°, 12.09°)	3	100	440

Formatted
Formatted
Formatted
Formatted
Formatted Table
Formatted
Formatted
Formatted
Formatted
Formatted
Formatted
Formatted
Formatted
Formatted
Formatted
Formatted
Formatted
Formatted
Formatted
Formatted
Formatted
Formatted
Formatted
Formatted
Formatted
Formatted
Formatted
Formatted
Formatted
Formatted
Formatted
Formatted
Formatted
Formatted
Formatted
Formatted
Formatted
Formatted
Formatted
Formatted
Formatted
Formatted

(DK0012R)								
Rucava (LV0010R)	Latvia	Filter-2pack Filter-1pack	Daily	1986-2020 (SO_2 from 1990)	(56.16°, 21.17°)	18	100	500
Schauinsland (DE0003R)	Germany	Filter-3pack	Daily	2000-2018	(47.91°, 7.91°)	1205	550	500
Tange (DK0003R)	Denmark	Filter-3pack Filter-2pack	Daily	1978-2020	(56.35°, 9.60°)	13	100	380
Tustervatn (NO0015R)	Norway	Filter-3pack Filter-2pack	Daily	1980-2020	(65.83°, 13.92°)	439	100	320
Utö (FI0009R)	Finland	Filter-3pack Filter-2pack Filter-1pack	Daily	1980-2020 (SO_2 from 1991)	(59.78°, 21.38°)	7	100	440
Valentia Observatory (IE0001R)	Ireland	Filter-3pack Filter-2pack	Daily	1980-2020	(51.94°, -10.24°)	11	100	320
Vavihill (SE0011R)	Sweden	Filter-3pack Filter-2pack Filter-1pack	Daily	1984-2015 (SO_2 from 1992)	(56.02°, 13.15°)	175	150	440
Virolahti II (FI0017R)	Finland	Filter-3pack Filter-2pack	Daily	1989-2014 (SO_2 from 1991)	(60.53°, 27.69°)	4	100	500
Waldhof (DE0002R)	Germany	Filter-3pack	Daily	2000-2018 (SO_4^{2-} from 2005)	(52.80°, 10.76°)	74	100	440
Zeppelin Mountain (NO0042G)	Norway	Filter-3pack	Daily	1990-2020	(78.91°, 11.89°)	474	350	440

185

Formatted
Formatted
Formatted

Station Name	Country	EMEP Station Code	Instrument Type/s	Freq.	Temporal Coverage	Lat. (N)	Lon. (E)	Alt. (m AMSL)	Trajectory Starting Height (m AGL)
Anholt	Denmark	DK0008R	Filter-3pack	Daily	1989-2020	56.71667	11.51667	40	100
Risoe	Denmark	DK0012R	Filter-3pack	Daily	2011-2020	55.69359	12.0858	3	100
Tange	Denmark	DK0003R	Filter-3pack Filter-2pack	Daily	1978-2020	56.35	9.6	13	100
Harwell	England	GB0036R	Online Ion Chroma.	Hourly	2009-2015 (SO_2 from 2011)	51.57306	-1.31667	137	100
Pallas Matorova	Finland	FI0036R	Filter-3pack Filter-2pack	Daily	1996-2020	68	24.23722	340	250
Utö	Finland	FI0009R	Filter-3pack Filter-2pack Filter-1pack	Daily	1980-2020 (SO_2 from 1991)	59.77917	21.37722	7	100
Virolahti II	Finland	FI0017R	Filter-3pack Filter-2pack	Daily	1989-2014 (SO_2 from 1991)	60.52667	27.68611	4	100
Neuglobsow	Germany	DE0007R	Filter-3pack Filter-1pack	Daily	1981-2018 (SO_2 from 2000)	53.16667	13.03333	62	100
Schauinsland	Germany	DE0003R	Filter-3pack	Daily	2000-2018	47.91472	7.90861	1205	550
Waldhof	Germany	DE0002R	Filter-3pack	Daily	2000-2018 (SO_4^{2-} from 2005)	52.80222	10.75944	74	100
Irafoss	Iceland	IS0002R	Filter-2pack Filter-1pack	Daily	1980-2020 (SO_2 from 2006)	64.08333	-21.01667	66	100
Valentia Observatory	Ireland	IE0001R	Filter-3pack Filter-2pack	Daily	1980-2020	51.93972	-10.24444	11	100
Rucava	Latvia	LV0010R	Filter-2pack Filter-1pack	Daily	1986-2020 (SO_2 from 1990)	56.16194	21.17306	18	100
Preila	Lithuania	LT0015R	Filter-3pack Filter-2pack	Daily	1991-2020	55.37611	21.03056	5	250

Table 1: Details of the 25 EMEP stations explored in this study which are shown geographically in Fig. 1. Stations highlighted in bold experienced at least one sulphurous pollution event between 1st September to 31st October 2014 attributed to Holuhraun emissions.

					(SO_2 from 1996)				
Birkenes II	Norway	NO0002R	Filter-3pack	Daily	2010-2020	58.38853	8.252	219	100
Hurdal	Norway	NO0056R	Filter-3pack	Daily	1997-2020	60.37239	11.07814	300	100
Kårvatn	Norway	NO0039R	Filter-3pack Filter-2pack	Daily	1980-2020	62.78333	8.88333	210	100
Tustervatn	Norway	NO0015R	Filter-3pack Filter-2pack	Daily	1980-2020	65.83333	13.91667	439	100
Zeppelin Mountain	Norway	NO0042G	Filter-3pack	Daily	1990-2020	78.90715	11.88668	474	350
Leba	Poland	PL0004R	Filter-2pack Filter-1pack	Daily	1993-2020	54.75389	17.53426	2	100
Auchencorth Moss	Scotland	GB0048R	Online Ion Chroma.	Hourly	2007-2020	55.79216	-3.2429	260	250
Aspvreten	Sweden	SE0012R	Filter-3pack Filter-2pack Filter-1pack	Daily	1984-2017 (SO_2 from 1988)	58.8	17.38333	20	100
Bredkälen	Sweden	SE0005R	Filter-3pack Filter-2pack Filter-1pack	Daily	1980-2020 (SO_2 from 1992)	63.85	15.334	404	100
Råö	Sweden	SE0014R	Filter-3pack	Daily	2002-2020	57.394	11.914	5	100
Vavihill	Sweden	SE0011R	Filter-3pack Filter-2pack Filter-1pack	Daily	1984-2015 (SO_2 from 1992)	56.01667	13.15	175	150

2.3 Numerical Model Simulations

Included in this study are Holuhraun eruption simulations by 5 GCMs: UKESM1.0, HadGEM3-GA7.0, MIROC6.1-SPRINTARS, ECHAM6.3-HAM2.3, and ECHAM6.3-HAM2.3-P3. Simulations are performed using the atmosphere-only component at a global scale (AMIP-style). To help clearly discriminate between signal and noise, the modelled horizontal winds and potential temperature are constrained ("nudged") to ERA-Interim reanalysis data (Dee et al., 2011) on a 6-hourly time scale, and use monthly observational datasets to prescribe sea surface temperature and sea ice boundary conditions (e.g. HadISST, Rayner et al., 2003). All other modelled variables evolve physically and dynamically as their setup dictates and are subject to the parameterisations in play. ~~Furthermore~~Also included in our inter-model comparison is~~,~~ ~~the global 3-D CTM~~ OsloCTM3, a global CTM ~~(Lund et al. 2018; Søvde et al., 2012) is included in this inter-model comparison~~. Unlike GCMs, CTMs do not simulate atmospheric dynamics explicitly, instead OsloCTM3 uses pre-calculated 3-hourly meteorological fields from ~~the European Centre for Medium-Range Weather Forecasts (~~ECMWF~~)~~ forecasts produced daily with a 12-hourly spin-up starting from ERA-Interim reanalysis. All numerical model simulations assume the eruption starts on 31st August 2014 and that the Holuhraun ~~that the~~ SO_2 emissions are distributed equally in the vertical for grid cells between 0.8 km and 3 km in the ~~grid cell~~ column containing the eruption vent following the magnitude and altitude profile of emissions described in Malavelle et al. (2017). All models include additional background SO_2 emissions from anthropogenic and natural sources. The simulations are continued from multiyear control simulations. All model output is regridded to a common regular 1.0° x 1.0° latitude-longitude grid using linear interpolation~~and are analysed at their native resolutions~~. Details specific to individual numerical models and key references can be found in Table 2.

Table 2: Details of the numerical models used in this study.

Model nName	Modelling cCentre	Chemistry/ Aerosol mModulee	Spatial RResolution (Lat. x Lon.)			Constraining / nudging data	References
			Atmospheric grid (lat. x lon.)	Surface layer thickness (m)	Levels within 3 km (AMSL)		
UKESM1UKESM1.0	Met Office Hadley Centre, UK	UKCA-Mode	N96 L85 (1.25° x 1.875°)	20	20	ERA-Interim	Mulcahy et al., 2020 Sellar et al., 2019 Dhomse et al., 2014
HadGEM3-GA7.0	Met Office Hadley Centre, UK	UKCA-Mode	N96 L85 (1.25° x 1.875°)	20	20	ERA-Interim	Mulcahy et al., 2020 Walterslliams et al., 20197 Dhomse et al., 2014
MIROC6.1-SPRINTARS	Research Institute for Applied Mechanics, Kyushu University, Japan	SPRINTARS	T213 L40 (0.5625° x 0.5625°)	45	13	ERA-Interim	Tatebe et al., 2019 Takemura et al., 2000, 2005, 2009
ECHAM6.3-HAM2.3	University of Oxford, UK	HAM (Default cloud microphysics scheme)	T63 L47 (1.875° x 1.875°)	68	9	ERA-Interim	Neubauer et al., 2019 Stevens et al., 2013 Tegen et al., 2019 Stevens et al., 2013
ECHAM6.3-HAM2.3-P3	ETH Zurich, Zurich, Switzerland	HAM-P3 (P3 cloud microphysics scheme)	T63 L47 (1.875° x 1.875°)	68	9	ERA-Interim	Dietlicher et al., 2018 Neubauer et al., 2019 Stevens et al., 2013 Tegen et al., 2019 Dietlicher et al., 2018 Stevens et al., 2013
OsloCTM3	CICERO Center for International	Stratospheric and	N80 L60 (2.25° x 2.25°)	10	16	ECMWF forecasts	Berntsen et al., 1997 Lund et al., 2018

Formatted: Centered

Formatted: Centered

Formatted: Centered

Formatted: Centered

Formatted: Centered

Formatted: Centered

Formatted: Centered

	Climate Research, Norway	N/Atropospheric chemistry schemes				(initiated with ERA-Interim)	Søvde et al., 2012

Table 2: Details of the numerical models used in this study.

2.4 Backward Trajectories

Lagrangian modelling has been used previously to study the long-range transport of Holuhraun pollutants (e.g. Boichu et al., 2019; Schmidt et al., 2015). Here~~T~~ the origin, age, and travel distance of~~he origin and age of~~ air ~~masses~~ parcels associated with sulphurous pollution events detected in the EMEP network observations are estimated using ~~air parcel~~backward single-particle trajectories generated by the Hybrid Single~~-~~Particle Lagrangian Integrated Trajectory (HYSPLIT) model developed by the National Ocean and Atmospheric Administration (NOAA) Air Resources Laboratory (Stein et al.~~,~~ 2015). We use 6-hourly ERA-Interim reanalysis data interpolated to an hourly resolution and regridded onto a 1.0° x 1.0° latitude-longitude grid as the meteorological input to the HYSPLIT model; a choice made to keep the driving meteorological data consistent between the trajectory analysis, and the nudging of the GCMs and CTM. Beginning on 1st September 2014 00:00 UTC, every hour at~~For~~ each EMEP station~~,~~ ~~-~~a new 27-member ensemble of 10-day backward trajectories is initiated ~~every hour at the altitudes~~ at the coordinates and altitudes listed in Table 1 ~~from 1st September to~~until the 31st October 2014 ~~31st October 2014~~ (a total of 1464 ensembles for each station) with locations along each trajectory saved hourly. ~~-~~The ERA-Interim reanalysis data for each ensemble is offset by a fixed grid factor, a maximum of 1.0° of latitude/longitude in the horizontal and 0.01 sigma units in the vertical, and so all the possible meteorological offsets result in the 27 members within each ensemble. ~~Subsequently~~As our ensembles are initiated at the beginning of every hour, pollution events ~~detected at stations sampling~~observed at a ~~sulphur concentration~~ daily resolution with a sampling midpoint centred on the hour have 25 ensembles ~~(one for every hour including the bounding hours of the sampling)~~ available for analysis ~~to evaluate an event's origin and age~~(12 hours either side of the midpoint and the midpoint itself), whilst ~~stations~~ those events ~~sampl~~observed~~ing~~ hourly with a sampling midpoint centred 30 minutes past the hour will have two2 ensembles (the bounding hours of the ~~sampling~~midpoint) ~~to utilise~~. This equates to a total of 675 and 54 individual trajectories respectively to evaluate the pollutant transport of each event~~. For consistency with the nudging of the models, ERA-Interim reanalysis data is used to run the HYSPLIT model which is applied at a regridded resolution of 1.0° x 1.0°~~.

~~-~~A limiting factor with using a backward trajectory analysis is that the trajectories are not expected to arrive exactly at the eruption vent. Subsequently, ~~and so~~ a domain must be defined that sets the bounds as to whether a trajectory is ~~where trajectories within are~~ deemed close enough ~~to the volcano~~ to be attributed to the volcano. Defining this domain can be done visually through satellite imagery (e.g. Pardini et al., 2017) or by a statistical analysis (e.g. Hughes et al., 2012)~~, yet it is not trivial to generalise (Witham et al., 2021)~~. Here we adopt the latter, defining multiple 3-D bounding cylinders centred on 64.85°N, 16.83°W with a height above mean sea level of 4.5 km and various bounding radii (see dotted regions in Fig. 1). The cylinder height is based on the maximum plume altitudes within the literature (Arason et al., 2015; Carboni et al., 2019a; Flower and Kahn, 2020; Pfeffer et al., 2018), whilst bounding radii are dependent on the distance from the eruption that the trajectories are initiated at. Trajectories released from stations distanced 1200–1500 km, 1500–1800 km, 1800–2100 km, and 2100–2400 km from Holuhraun are subject to radii of 320 km, 380 km, 440 km, and 500 km respectively. These values are

Formatted: Superscript

Formatted: Not Highlight

Formatted: Not Highlight

Formatted: Not Highlight

Formatted: Not Highlight

based on the positional error of a trajectory being approximately 10–30% of the total distance travelled (Stohl, 1998). A special case is made for the Irafoss station due to its close proximity to Holuhraun (~200 km). Over this distance, due to the finite hourly resolution of the trajectories and magnitude of local wind speeds, a trajectory is likely to travel further in a single time step than the estimate obtained from the "10–30% distance travelled" method. Subsequently, even an ideal trajectory passing directly over the eruption may not be outputted within the bounding radius. Consequently, to ensure a near 100% likelihood these ideal trajectories are captured, we define the Irafoss radius as the 99th percentile of the September and October ERA-Interim reanalysis horizontal wind speeds of the grid cells containing the horizontal eruption location and with midpoints below the cylinder height (see Supplement, S1).

This study attributes an observed sulphurous pollution event to volcanic emissions from Holuhraun when at least 25% of the released trajectories pass through the relevant 3-D bounding cylinder, equating to a minimum of 167 and 14 trajectories for daily and hourly sampled events respectively. Whilst this threshold could be considered low allowing for other sources to contribute to the sulphurous pollution detected, the sheer volume of Holuhraun emissions within the region versus other sources during September and October 2014, and the rural location of the surface stations, gives confidence that this threshold is sufficient. We average the transport time and travel distance of the individual trajectories attributed to Holuhraun at their point of closest approach to the eruption to estimate the age and distance travelled by the plume at a given pollution event. The error in the plume age is estimated as the larger value of either the standard error of the trajectories sampled or the trajectory temporal resolution (1 h).

Like all frameworks based on single-particles trajectories, our trajectory analysis is subject to the inherent uncertainty associated with individual trajectories (Stohl, 1998) with the uncertainty in the input meteorology often regarded as the dominant contribution (Engström and Magnusso, 2009; Gebhart et al., 2005; Harris et al., 2005). Here we minimise this main cause of uncertainty by perturbing the meteorology for each ensemble member. However, other uncertainties, such as the choice of meteorological dataset and/or trajectory model, and the exclusion of turbulence, have not been accounted for in our trajectory framework. Although these uncertainties are relevant, the focus of this study is to inter-compare numerical models consistently rather than through a rigorous dispersion exercise, and so they will not be considered further. Despite the simplicity of our single-particle trajectory framework, similar methods have been applied successfully to surface monitoring stations (e.g. Nieminen et al., 2015; Räty et al., 2023; Väänänen et al., 2013).

Formatted: Not Highlight

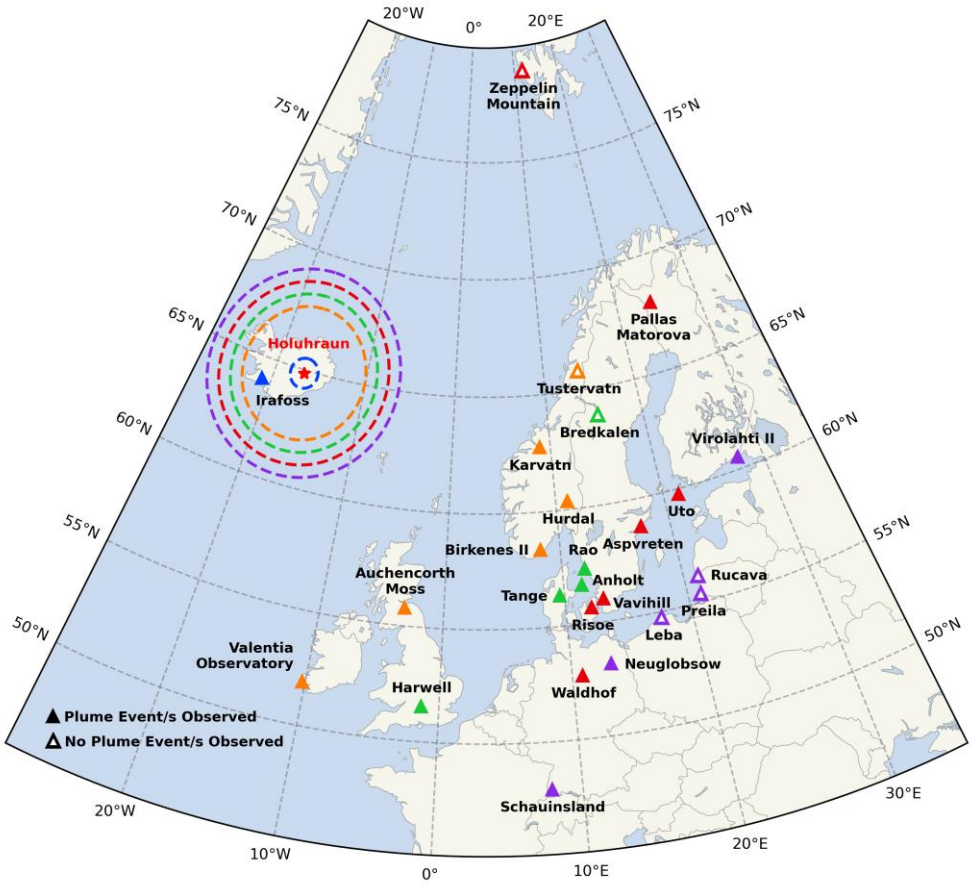

~~Here we define this domain as a 3-D bounding box in the Holuhraun vicinity (20.33°W to 13.33°W, 63.35°N to 66.35°N, 0-4.5 km AMSL – see Fig. 1) and events with at least 2% of released trajectories passing through are attributed to volcanic emissions. The transport time of this subset of volcanically influenced events, essentially the age of the plume at the point of observation, are calculated using an averaging procedure. This procedure begins by considering only trajectories passing through the 3-D bounded domain (e.g. the red idealised trajectories in Fig 1.). For each of these trajectories, the age of the individual trajectory points residing in the bounding box (e.g. black circles in Fig 1.) are averaged resulting in the average transport time from the immediate Holuhraun vicinity to the EMEP station for a single trajectory. Finally, the transport time of the event, the plume age at the time of sampling, is calculated as the average of these individual single trajectory transport times (e.g. the average transport time of the two red idealised trajectories in Fig. 1).~~

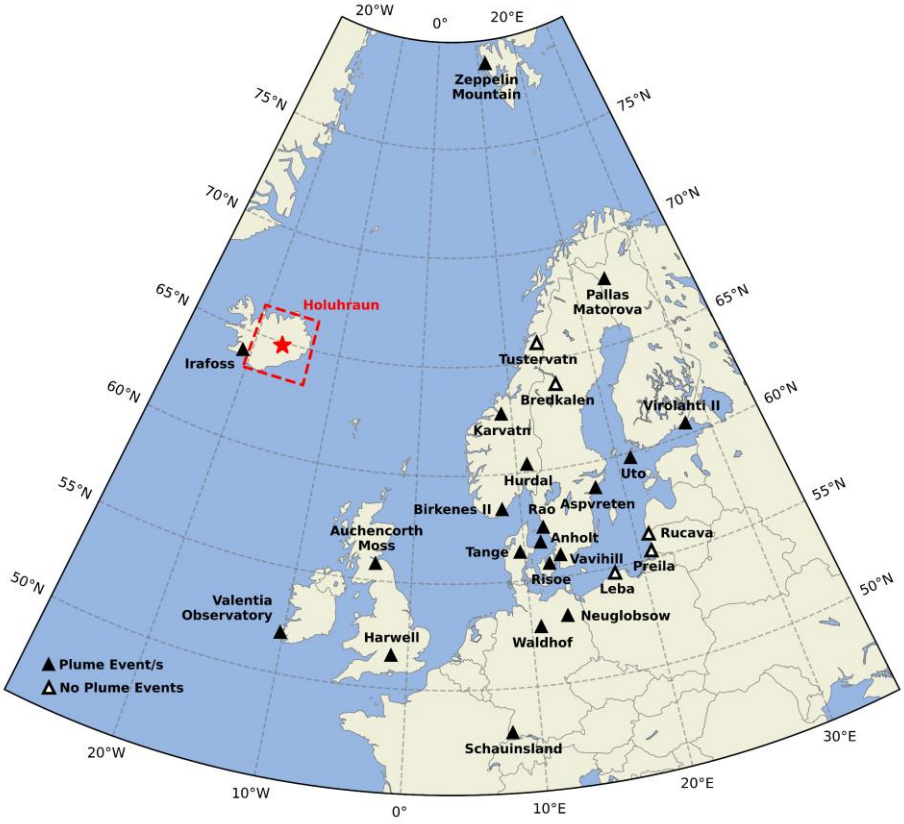

Figure 1: Map of the 25 EMEP stations explored in this study. Stations marked with filled triangles experienced at least one sulphurous pollution event between 1st September to 31st October 2014 attributed to Holuhraun emissions, whereas stations marked with unfilled triangles did not.~~. Stations marked with unfilled triangles either experienced no sulphurous pollution events or only events attributed to other sulphurous sources.~~ A red star indicates the location of the Holuhraun eruption (64.85°N, 16.83°W) with the surrounding ~~red~~ dashed line~~s~~ outlining the horizontal boundaries of the Holuhraun bounding area~~svicinity~~ defined in this study ~~(20.33°E to 13.33°W, 63.35°N to 66.35°N)~~. From the inner circle outwards, the radii are: 72 km, 320 km, 380 km, 440 km, and 500 km. Colouring links a station to the bounding area it is subject to. ~~Dotted lines show idealised backward trajectories initiated at Pallas Matorova for a single sulphurous pollution event with red and black lines~~

representing trajectories that would and would not be attributed to the Holuhraun eruption respectively. Black circles represent idealised trajectory points that fall within the bounded Holuhraun vicinity.

~~3 SO2 Plume Distribution, Height, and Mass Burden~~

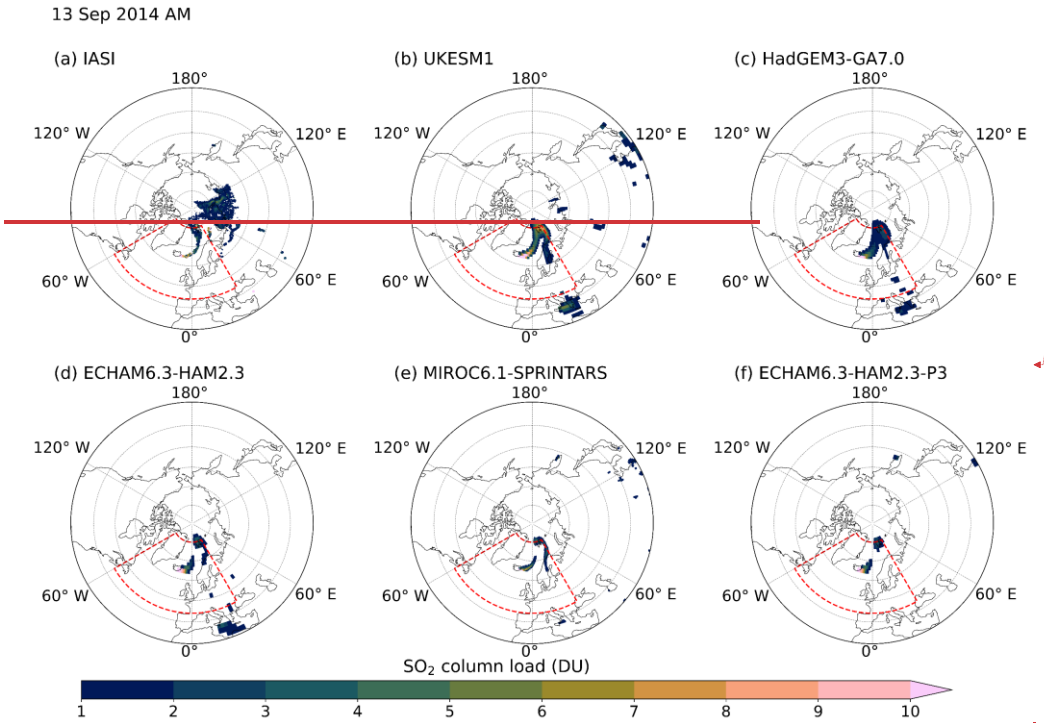

3. SO_2 Plume Spatial Distribution

Formatted: Highlight

Formatted: Heading 1

Formatted: Subscript

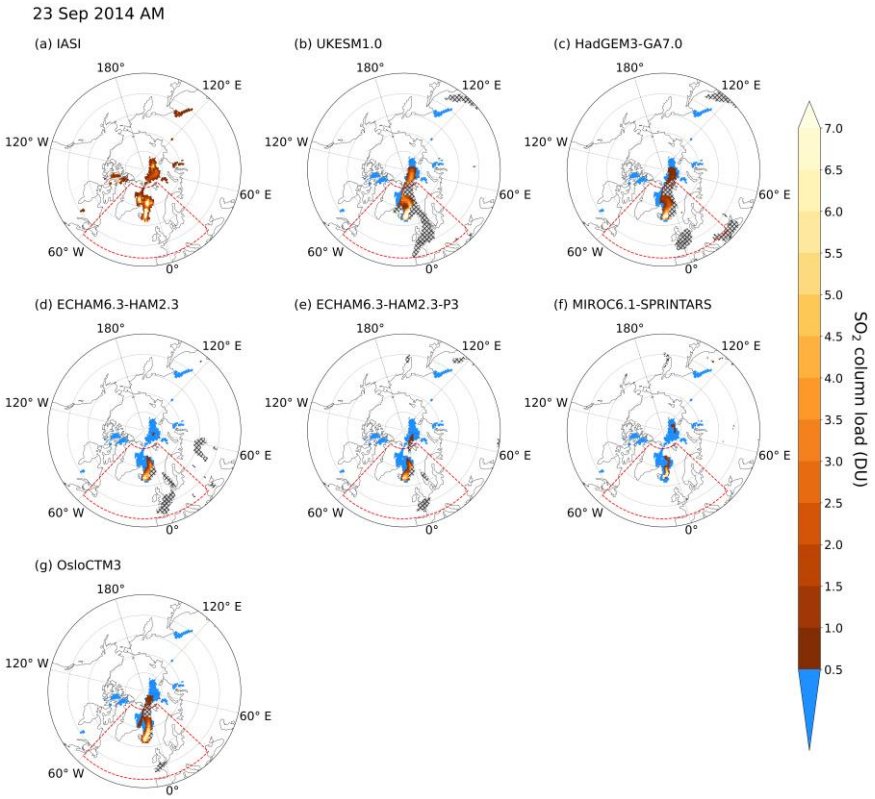

Figure 2: SO_2 column load from (a) Infrared Atmospheric Sounding Interferometer (IASI) retrievals and (b, c, d, e, f, g) model simulations of the Holuhraun eruption on the 23rd September 2014 AM. IASI data below 0.5 Dobson units (DU) are masked to identify the observed plume extent. Model output is sampled at 09:30 UTC. Non-hatched areas show model output within the observed plume extent with the distinct blue highlighting model values below the 0.5 DU threshold. Hatched areas show model output outside the observed plume extent that are above the 0.5 DU threshold. Both IASI and model data have been regridded onto the same 1.0° x 1.0° latitude-longitude grid. Red dashed areas represent the Holuhraun region defined in this study. An animation of September and October 2014 can be found in the Supplement (S2).

Formatted: Not Highlight

The SO_2 column load from IASI retrievals and model simulations on the 23rd September 2014 AM are displayed in Fig. 2 and an animation spanning September and October 2014 can be found in the Supplement (S2). We mask IASI SO_2 column load retrievals below 0.5 DU to identify the observed horizontal extent of the plume. This threshold sufficiently exceeds the region's

Formatted: Not Highlight

typical background SO_2 column load of approximately 0.1 DU; a background derived using the 2007–2009 September mean SO_2 mass burden of a similar geographical region given in Schmidt et al. (2015). Applying such a threshold ensures enough SO_2 from other sources are screened out whilst not removing data associated with the main volcanic plume. To enable a comparison with the IASI retrievals, the model output is regridded onto the same 1.0° x 1.0° latitude-longitude grid and is sampled within the observed plume extent at 09:30 UTC and 21:30 UTC for the AM and PM grouped retrievals respectively. Areas within the observed plume extent that the models fail to capture (i.e. values below 0.5 DU) are shown in a distinct blue.

Within the Holuhraun region (red dashed area) in Fig. 2, UKESM1.0, HadGEM3-GA7.0 and OsloCTM3 perform well in capturing the observed plume extent with minimal blue areas present, whilst the ECHAM variants and MIROC6.1-SPRINTARS roughly capture 50% and 30% respectively. These performances largely hold true across September and October as evident in the animation. Although, due to the binary nature of the observed plume extent masking, no magnitude on how far the modelled values lie below 0.5 DU is given and so this metric should not be considered a sole indicator of model performance. In addition, we sample the models outside the observed plume extent when the modelled SO_2 column load exceeds 0.5 DU (hatched areas). In Fig. 2 all models except MIROC6.1-SPRINTARS simulate the plume outside the observed area over parts of Western Europe. These areas potentially arise due to IASI retrieval limitations causing parts of the plume to be missed (e.g. cloud cover, high latitude, swath width) or due to high levels of background SO_2 emissions in the models (e.g. volcanic activity from Mt. Etna, anthropogenic activity). In September, for UKESM1.0, HadGEM3-GA7.0, and OsloCTM3 the hatched areas tend to dominate the blue areas suggesting that their modelled plume areas are greater than the IASI retrievals, whereas the opposite is true for the remaining models. In October, all models largely show a greater modelled plume area than observed, yet this is partly due to the low IASI coverage across this period.

Overall, Fig. 2 and the animation make it apparent that the Holuhraun eruption is observed and modelled as the main source of SO_2 in our region of interest. Contributions from high background SO_2 sources are minimal relative to the total regional SO_2 and occur either outside or just within the outer bounds of the region, so are unlikely to substantially influence this study. Both visualisations show that the models capture the general features of the observed plume, particularly the dispersion over the Fennoscandian Peninsula and the UK during September, suggesting that nudging the models to ERA-Interim reanalyses gives credence to the models' ability to accurately simulate the plume dispersion despite their coarse resolution. It is worth noting that the animation shows possible regridding artefacts in the IASI retrievals on the 11th, 12th, and 17th September PM. These artefacts occur outside our region of interest and so will not be considered further here.

Figure 2: Comparison of volcanic SO_2 column load from (a) Infrared Atmospheric Sounding Interferometer (IASI) retrievals and (b, c, d, e, f) model simulations of the Holuhraun eruption on the morning of 13th September 2014. Red dashed area represents the Holuhraun region (44°N to 80°N, 60°W to 30°E) defined in this study. The model output is sampled at 09:00 UTC and 21:00 UTC for the AM and PM bidaily groups respectively. Observed and simulated SO_2 column loads below 1 DU are masked to identify in-plume areas. IASI data and model output are shown on a 0.125° x 0.125° grid and at the resolutions given in Table 2 respectively. A full animation between 1st September to 31st October 2014 can be found in the Supplement (S1).

~~The bidaily SO_2 column load from the IASI retrievals and the model simulations between 1st September to 31st October 2014 feature in the animation in Supplement (S1) and the morning snapshot of the 13th September displayed in Fig. 2. The model output is sampled at 09:00 UTC and 21:00 UTC for the AM and PM bidaily grouped retrievals respectively. Observed and simulated SO_2 column loads below 1 DU are masked to identify in-plume areas as is done in other Holuhraun studies (e.g. Haghighatnasab et al., 2022). This threshold is somewhat arbitrary yet strikes an acceptable balance in screening out enough SO_2 from other sources within the red dashed Holuhraun region whilst not removing data associated with the main volcanic plume. From Fig. 2 and the animation it is apparent that the Holuhraun eruption is observed and modelled as the main source of SO_2 in the region, yet small areas of background SO_2 exist despite the plume detection screening (e.g. volcanic activity from Mt. Etna). However, the contribution from these high background SO_2 sources relative to the total regional SO_2 is minimal and unlikely to influence this study. Outside the Holuhraun region other SO_2 sources are more noticeable, such as volcanic activity from the Kamchatka Peninsula and anthropogenic activity in Norilsk, Russia, yet their distances from the area of interest mean they do not need to be considered further here. Both visualisations show that the models capture the general features of the observed plume, particularly the dispersion over the Fennoscandian Peninsula and the UK during September, suggesting that nudging the models to ERA-Interim reanalyses gives credence to the models' ability to accurately simulate the plume dispersion despite their coarse resolution. The models often have larger plume areas, yet this is likely due to IASI retrieval limitations (e.g. cloud cover, high latitude, swath width) rather than an overestimation. Despite supplementing the MetOp-A IASI retrievals with that of MetOp-B, IASI coverage is limited during 17th–18th September and 9th–11th, 18th–19th, and 30th–31st October. Care should be taken when comparing IASI retrievals to the models across these dates.~~

4. SO_2 Plume Height and Mass Burden

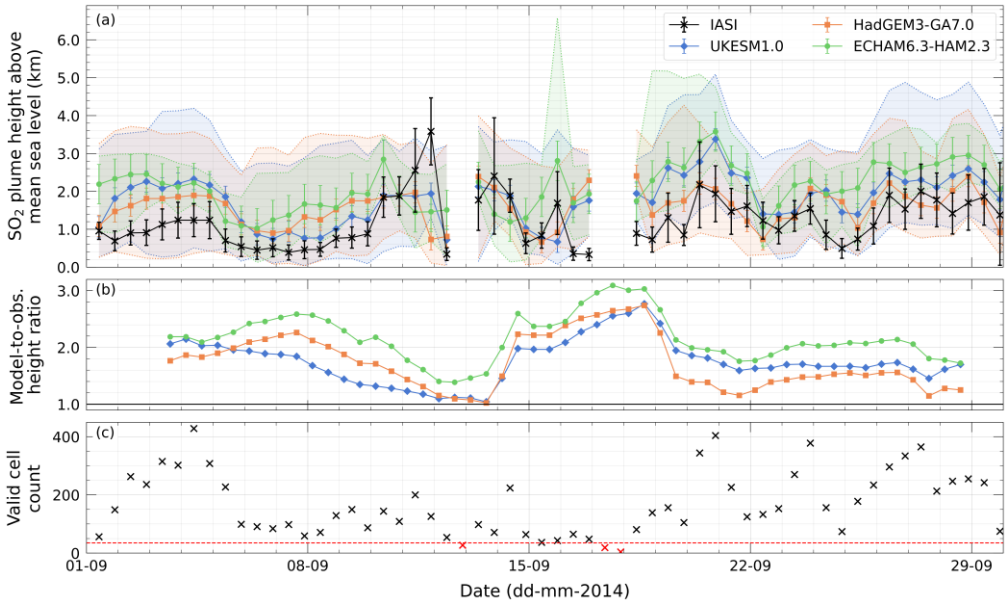

Formatted: Heading 1

Formatted: Subscript

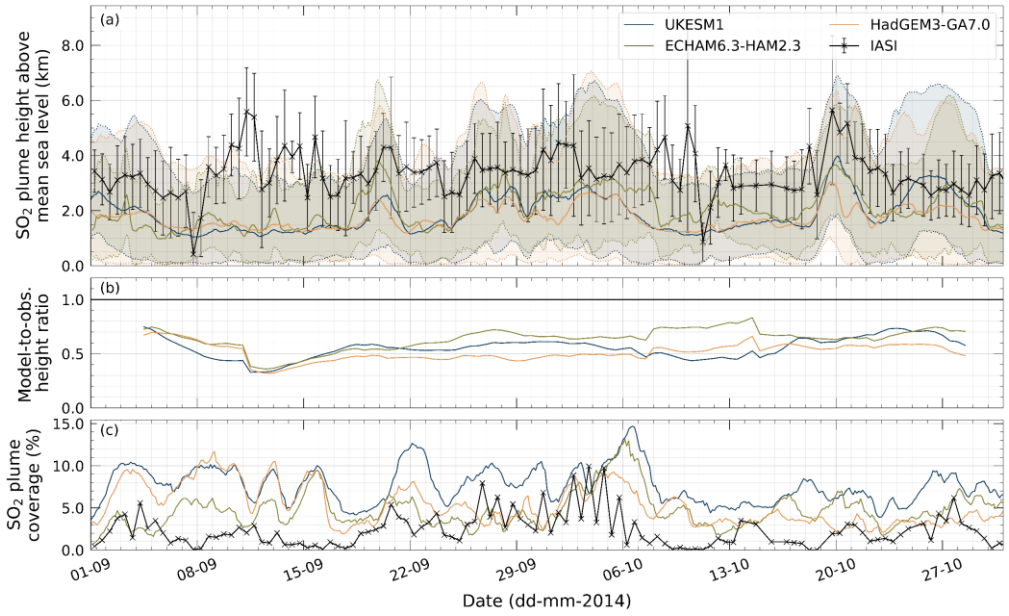

385

Formatted: Left, Line spacing: single

Figure 3: (a) ~~Instantaneous~~ Bidaily temporal evolution and (b) ~~5~~7-day rolling mean of IASI retrieved and modelled ~~plume~~ 390 SO_2 plume heights across the Holuhraun region (44°N to 80°N, 60°W to 30°E) for September 2014~~rom 1st September to 31st October 2014~~. Black crosses and error bars represent the regional mean IASI SO_2 plume height and associated ~~retrieval~~ error. ~~Modelled~~ Models are sampled only within the observed plume extent and their SO_2 plume heights are shown as a vertical profile. The ~~solid~~ coloured lines and error bars represent the regional mean ~~modelled~~ central height of the SO_2 plume and associated error, whilst~~and~~ an ~~the associated~~ envelope indicates the regional mean height of the top and bottom ~~derived top~~ 395 ~~and bottom regional mean heights of~~of the SO_2 plume (see text). The 5-day rolling means tolerate a maximum of two missing data points. ~~.~~ (c) ~~The~~ Number of grid cells used to calculate the regional means~~area the SO_2 plume covers as a percentage of the total Holuhraun region from 1st September to 31st October 2014~~. The red dashed line indicates the~~,~~ minimum number of grid cells deemed sufficient to enable a fair comparison between observed and modelled. Both IASI and model data have been regridded onto the same 1.0° x 1.0° latitude-longitude grid.

400

The average observed and modelled ~~and modelled~~ SO_2 plume height~~s~~ across the Holuhraun region f~~or~~ September and October 2014 are~~rom 1st September to 31st October are~~ shown in Fig. 3a and the Supplement (S3) respectively, with ~~are~~ monthly values provided~~summarised~~ in Table 3. The IASI retrievals show that the observed SO_2 plume height, specifically the central height of a Gaussian SO_2 vertical profile, exists primarily (~75~~80~~%) between 0.8~~2.5~~ 2.5~~4~~ km above mean sea level, very rarely exceeding 3~~5~~ km, showing that the volcanic perturbation to the region is contained well within the lower troposphere~~. On the morning of 1st September, the observed plume area (see animation in Supplement, S1) is centred close to the vent suggesting that the IASI retrieved height of 3.4 km is a good estimate for the plume injection height on this day.~~ ~~Fig. 3a shows t~~The modelled SO_2 plume vertical ~~profiles across the Holuhraun region~~profiles are determined from model output that has been subject to the same sampling used in Sect. 3, plus an additional masking in the vertical of grid cells with ~~that are determined from the vertical cells within the in-plume areas with~~ SO_2 mass concentrations ~~exceeding~~ below 4.5~~1~~ μgm^{-3}; a threshold based on the clean air SO_2 concentration of 1 ppbv (roughly 3 μgm^{-3} at 2–3 km) given in Theys et al. (2013). From the remaining grid cells with sufficient concentrations in the observed plume extent, ~~T~~the modelled central SO_2 plume height, ~~given~~ represented by a solid line, is calculated as the regional mean of the heights of the grid cells containing the maximum SO_2 concentration in each column. The associated error is based on the typical vertical resolution of the model between 2–4 km above mean sea level. ~~is the regional average of the mean cell height of those vertical cells above the threshold.~~ The top and bottom of the modelled SO_2 plume ~~heights~~, ~~represented~~ illustrated by the outer dotted lines enclosing the envelope, are the regional averages of the maximum and minimum ~~cell~~ heights of ~~those vertical cells~~the sufficiently polluted grid cells ~~above the threshold~~. Fig. 3c shows the underlying number of data points contributing to the regional means. Regional means calculated from a number of data points below the minimum threshold of 35 (red dashed line) are deemed inadequate for a fair comparison and do not contribute to the rolling means shown in Fig. 3b. Note, from the output provided to this experiment, ECHAM6.3-HAM2.3-P3 and MIROC6.1-SPRINTARS SO_2 plume heights can only be compared with IASI retrievals at a monthly resolution, whereas no comparison is possible for OsloCTM3.

~~Generally, the models~~UKESM1.0, HadGEM3-GA7.0, and ECHAM6.3-HAM2.3 ~~slightly over~~~~under~~estimate the central plume height ~~for most of~~ across September as clearly evidenced ~~and October as shown i~~in the 5~~7~~-day rolling mean model-to-observed ~~ratio in Fig. 3b~~ratio. This over~~under~~estimation is greatest during the third~~second~~ week, ~~of September~~ particularly on the~~when even the top heights of the modelled vertical profiles are below the observed peaks across~~ 16~~1~~th and~~to~~ 18~~4~~th September. ~~This feature may be a consequence of the vertical winds in the models not being constrained and/or additional variability in the momentum flux during the onset of the~~ the eruption which is not accounted for in the prescribed emission profile used in the models. The observed variability in the plume height is largely well represented in the three models with all peaks, aside from the 11th September PM, captured within error whilst the observed central height is very rarely found outside the modelled vertical profiles. ~~From mid-September onwards the models' ability to capture the variability in plume height improves lying mostly within the estimated observational error.~~ The bottoms of the modelled vertical profiles~~volcanic plumes~~ are close to the

Formatted: Not Highlight
Formatted: Subscript
Formatted: Not Superscript/ Subscript
Formatted: Subscript
Formatted: Subscript
Formatted: Superscript

surface suggesting that ground-based stations within the region are likely to experience moments of sulphurous pollution due to the eruption. The performance of the three models during October is similar (see Supplement, S3), although the limited IASI retrievals make comparison harder. On a monthly scale, Table 3 indicates that all models where comparison is possible agree with the mean September and October observed heights within error, providing confidence that the models ~~during September and October. Fig. 3c presents the in-plume area as a percentage of the Holuhraun region. The previous assessment that the modelled plumes occupy a greater area than the IASI plume is quantitively supported here. Fig. 3c shows that the sharp peaks and troughs in the observed plume height on 7th September and 10th, 11th, and 18th October occur during periods when the IASI coverage is very low and so may not reflect the height of the complete plume. The ECHAM6.3-HAM2.3-P3 simulation does not have the required output to estimate the SO_2 plume vertical profile at a bidaily resolution, yet the monthly mean central height shown in Table 3 of 1.8 km is close to the observed range which gives some confidence the model~~ adequately capture~~s~~ the plume height within the Holuhraun region at this temporal resolution.

Formatted: Not Highlight

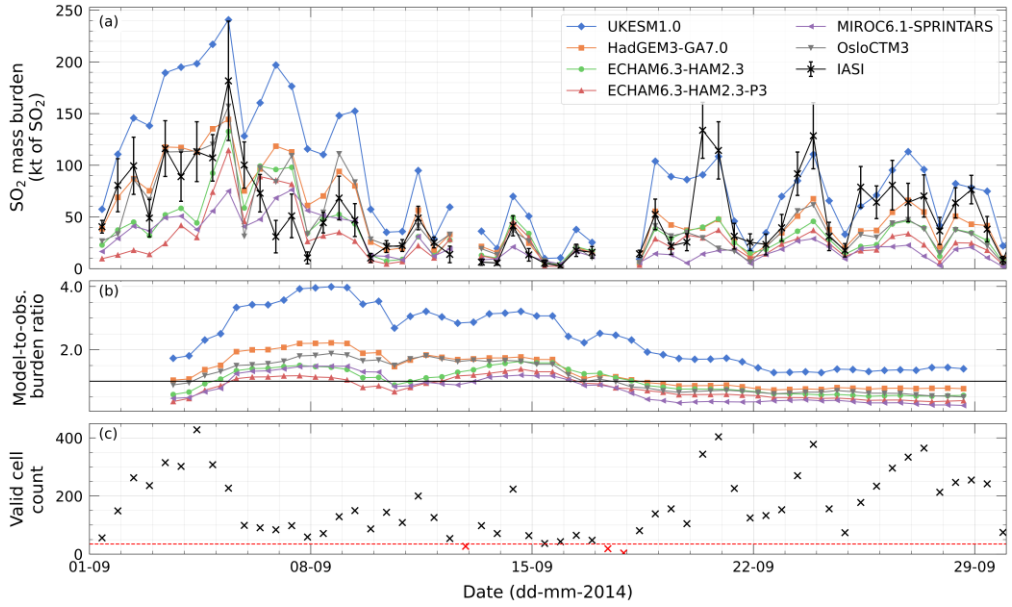

~~Note that MIROC6.1-SPRINTARS simulation does not have the required output to estimate the SO_2 plume vertical profile.~~**Figure 4:** (a) Bidaily temporal evolution and (b) 5-day rolling mean of IASI retrieved and modelled SO_2 mass burdens across the Holuhraun region (44°N to 80°N, 60°W to 30°E) for September 2014. Black crosses and error bars represent the mass burdens and associated error derived from the IASI retrievals. Models are sampled only within the observed plume extent and their derived mass burdens are given by the coloured lines. The 5-day rolling means tolerate a maximum of two missing data points. (c) Number of grid cells used to calculate the mass burdens. The red dashed line indicates the minimum number of grid cells deemed sufficient to enable a fair comparison between observed and modelled. Both IASI and model data have been regridded onto the same 1.0° x 1.0° latitude-longitude grid.

The IASI retrieved and modelled SO_2 mass burdens across the Holuhraun region for September and October 2014 are shown in Fig. 4a and ~~from 1st September to 31st October are summarised in Table 3 with the time series provided in the Supplement (S2). the~~ Supplement (S4) respectively, with monthly values provided in Table 3. Both t~~T~~he observed and modelled~~SO_2~~ mass burdens are ~~obtained~~ derived by summing the product ~~of the of the individual in-plume pixel/grid cell~~ SO_2 column loads and

Formatted: Font: Bold
Formatted: Subscript
Formatted: Not Highlight
Formatted: Not Highlight

surface area of the individual grid cells within the observed plume extent for each bidaily interval. ~~and corresponding surface area across the region for each time step.~~ The same method is applied to ~~to~~ the SO_2 column load IASI retrieval error to estimate an SO_2 mass burden observational error. For September and October 2014, we estimate an ~~Across September and October, the~~ average bidaily SO_2 mass burden of 52 ± 15 ~~from IASI is 63 ± 23~~ kt of SO_2 and 34 ± 9 kt of SO_2, from IASI retrievals respectively which is in excellent agreement with Malavelle et al. (2017) who report corresponding mass burdens of 52 kt of SO_2 and 30 kt of SO_2 using an independent IASI dataset for the same geographical region. September mass burdens derived in Schmidt et al. (2015) using the Ozone Monitoring Instrument (OMI) are considerably higher, averaging 99 ± 49 kt of SO_2, across a slightly smaller area (45°N to 75°N, 60°W to 30°E). There exists ~~, yet there is~~ substantial bidaily variation in the observed mass burden evident by the peaks of 180~~204~~ ± 6~~01~~ kt of SO_2, 130~~79~~ ± 30~~55~~ kt of SO_2, and 16~~3~~0 ± 30~~47~~ kt of SO_2 on 5th, 20th, and 23rd September respectively, and the low values below 15~~0~~ kt of SO_2 (e.g. 13~~7~~th, ~~and~~ 16~~5~~th September~~, 10th and 18th October~~). ~~This~~ variation is likely caused by a combination of the plume passing in and out of the defined region, ~~and~~ changing IASI retrieval coverage (see Fig. 3c and 4c), and fluctuations in the volcanic ~~as opposed to physical or chemical processes, such as substantial fluctuations in the volcanic~~ SO_2 emission flux (Thordarson and Hartley, 2015).~~.~~

With respect to the models, HadGEM3-GA7.0, ECHAM6.3-HAM2.3, and OsloCTM3 simulate ~~The models simulate an~~ average bidaily SO_2 mass burdens that lie close to those of the IASI retrievals for September and October 2014. UKESM1.0 overestimates the observed mass burdens, particularly during the early stages of September, which is potentially due to overpredicting total column SO_2; a bias that has been noted previously (Hardacre et al., 2021). As the IASI instrumentation is not able to sample the full intricacies of the plume, the observed SO_2 mass burden presented here is to be considered as a lower estimate and so UKESM1.0 exceeding this total may not necessarily be an indicator of poor performance. ECHAM6.3-HAM2.3-P3 and MIROC6.1-SPRINTARS largely underestimate the IASI derived mass burdens, yet as the models are only sampled within the observed plume extent, these two models, as well as the remaining models, may simulate considerable mass in regions outside this extent (hatched areas in Fig. 2 and animation, S2). ~~in agreement with that derived from the satellite instrumentation, aside from UKESM1 and MIROC6.1-SPRINTARS that respectively overestimate and underestimate the IASI derived totals. As the IASI instrumentation is not able to sample the full intricacies of the plume, the SO_2 mass burden presented here is to be considered as a lower estimate and so UKESM1 exceeding this may not necessarily be an indicator of poor performance.~~ All models capture the observed variability, simulating larger mass burdens during early ~~simulate a maximum SO_2 mass burden in Se~~September when the eruption is most powerful and prescribed emission rates the highest, before decreasing during October. ~~illustrating that they capture the observed variability well. Interestingly, there is a noticeable range in the general magnitude of the simulated mass burdens despite each model using the same prescribed emission profile.~~ Correcting the IASI retrievals for parts of the SO_2 plume potentially missing has proved valuable (e.g. Carboni et al., 2019a) and could improve the comparison of~~agreement with~~ the modelled heights and mass burdens presented here, yet as the general variability of both characteristics is well captured and no significant defects exist, using a cloud-adjusted correction is deemed unnecessary here.

Formatted: Font: 10 pt, Font color: Auto
Formatted: Font: 10 pt, Font color: Auto, Subscript
Formatted: Font: 10 pt, Font color: Auto
Formatted: Subscript
Formatted: Not Superscript/ Subscript
Formatted: Font: 10 pt, Font color: Auto
Formatted: Subscript
Formatted: Subscript
Formatted: Not Highlight

~~Note the OsloCTM3 simulation does not have the required diagnostics to compare the SO_2 plume evolution with IASI retrievals.~~

Table 3: Monthly IASI retrieved and simulated SO_2 plume heights and SO_2 mass burdens across the Holuhraun region (44°N to 80°N, 60°W to 30°E) for September (S) and October (O) 2014. Plume heights for MIROC6.1-SPRINTARS and ECHAM6.3-HAM2.3-P3 are derived from monthly resolution sampling, rather than bidaily as is done for other model estimates. The OsloCTM3 simulation does not contain the required diagnostics for a plume height estimate.

			IASI	~~UKESM1~~UKESM1.0	HadGEM3-GA7.0	MIROC6.1~~.~~-SPRINTARS	ECHAM6.3-HAM2.3-P3	ECHAM6.3-HAM2.3	OsloCTM3
SO_2 pPlume ~~Altitude~~ height (km AMSL)	~~MaxM~~ean~~.~~	S	1.2~~5.6~~ ± 0.5~~2.7~~	1.8 ± 0.3~~4.0~~	1.6 ± 0.3~~3.1~~	1.1 ± 0.5~~-~~	1.8 ± 0.5~~-~~	~~3.8~~2.1 ± 0.5	-
		O	1.7 ± 0.7	2.3 ± 0.3	2.2 ± 0.3	1.5 ± 0.5	2.1 ± 0.5	2.7 ± 0.5	-
	Maxin~~.~~	S	3.6 ± 0.9~~0.4~~ ± 1.5	3.8 ± 0.3~~1.0~~	2.7 ± 0.3~~1.2~~	2.8 ± 0.5~~-~~	~~-~~2.5 ± 0.5	~~1.0~~3.6 ± 0.5	-
		O	3.2 ± 1.5	4.2 ± 0.3	4.8 ± 0.3	2.7 ± 0.5	2.8 ± 0.5	4.1 ± 0.5	-
	Min.e~~an~~	S	0.33 ± 0.16~~3.4 ± 1.4~~	0.7 ± 0.3~~1.9~~	0.7 ± 0.3~~1.7~~	0.3 ± 0.5~~-~~	~~1.8~~0.5 ± 0.5	~~2.1~~1.0 ± 0.5	-
		O	0.20 ± 0.13	0.6 ± 0.3	0.6 ± 0.3	0.5 ± 0.5	0.7 ± 0.5	1.4 ± 0.5	-
SO_2 mMass bBurden (kt of SO_2)	Meana~~x.~~	S	52~~204~~ ± 15~~61~~	88~~393~~	51~~225~~	25~~109~~	27~~128~~	36~~176~~	44~~-~~
		O	34 ± 9	45	26	13	22	30	23
	Maxin.	S	1800.10 ± 60.04	24~~169~~	144~~29~~	76~~7~~	114~~9~~	133~~18~~	157~~-~~
		O	230 ± 20	112	68	37	61	76	57
	Min.e~~an~~	S	2.6~~63~~ ± 1.1~~23~~	9.2~~171~~	2.9~~86~~	1.7~~35~~	2.1~~55~~	4.3~~76~~	1.2~~-~~

Formatted Table

		O	1.8 ± 1.1	2.2	1.4	0.1	0.6	1.9	0.9

Table 3: IASI retrieved and simulated SO_2 plume altitude and SO_2 mass burden across the Holuhraun region (44°N to 80°N, 60°W to 30°E) from 1st September to 31st October 2014.

510

Formatted: Heading 1

54 Sulphurous Surface Mass Concentrations

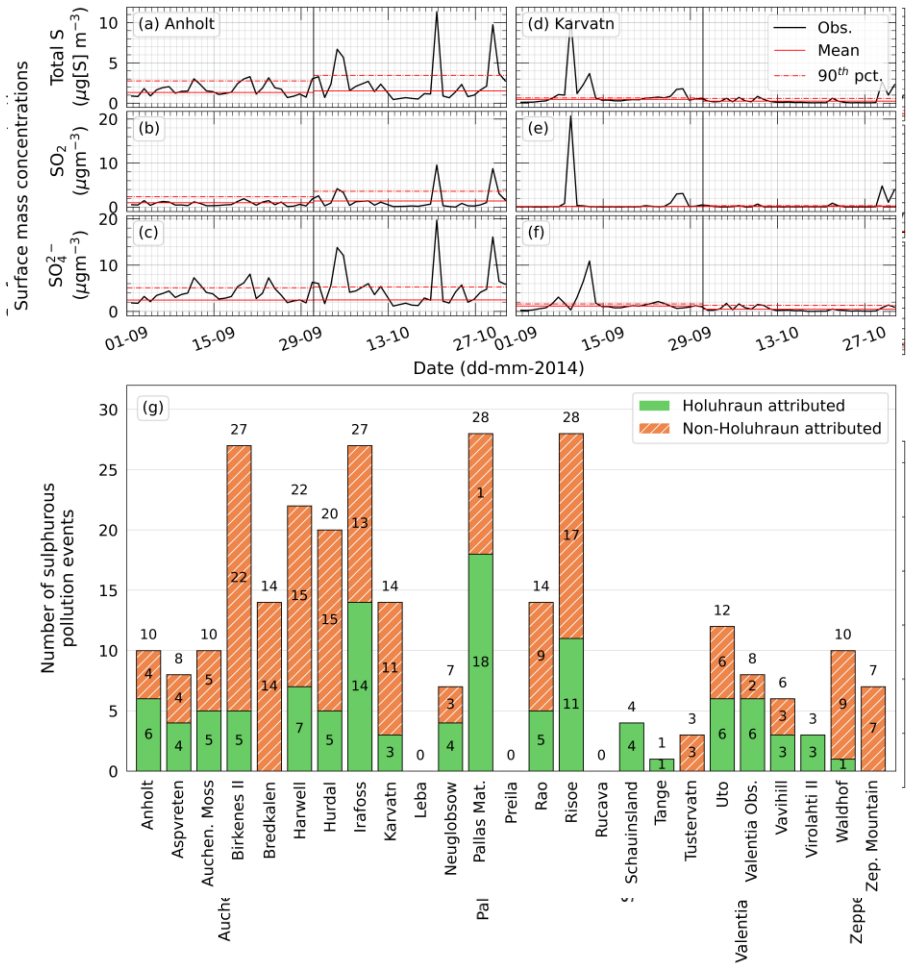

Figure 54: Observed surface mass concentration time series of total sulphur content, SO_2 and SO_4^{2-} at (a, b, c) Anholt (Denmark) and (d, e, f) Kårvatn (Norway) between 1st September and 31st October 2014. Climatological monthly mean and 90th percentile values are given in the red solid and dashed lines respectively. (g) ~~Number of sulphurous~~Sulphurous pollution

Formatted: Normal

events (see Sect. 2.2) identified across the 25 EMEP stations highlighting those attributed to ~~categorised in terms of those attributed to~~ Holuhraun emissions (green solid fill) and those not ~~attributed to other sulphurous sources~~ (orange hashed fill).

Observed time series of surface mass concentrations of total sulphur content, SO_2 and SO_4^{2-} from 1st September to 31st October 2014 at EMEP stations Anholt (Denmark) and Kårvatn (Norway) are shown in Fig. 4a-c and Fig. 4d-f respectively. Time series of the remaining~~other 23~~ EMEP stations are provided in the Supplement (S~~53-27~~25). Anholt and Kårvatn feature numerous peaks in sulphurous concentrations that exceed the climatological monthly statistics suggesting that these concentrations are significant and, given the~~ir~~ rural locations of the sites, are likely caused by far afield sources of pollutants. Using the definition given in Sect. 2.2, we find that Anholt experienced 10 pollution events during September and October whilst Kårvatn experienced 14. We see merit in defining a pollution event using the total sulphur content concentration, rather than the commonly used SO_2 concentration (e.g. Boichu et al., 2019), as additional events are identified due to their high SO_4^{2-} concentrations which otherwise would have been missed (e.g. ~~Anholt on 19th,~~ 20th and 23rd September at Anholt, ~~Kårvatn on 11th and 1~~12th September at Kårvatn). The number of ~~Fig. 4g displays the number of~~ sulphurous pollution events observed across the ~~selected~~25 ~~25~~ EMEP stations during September and October 2014 is shown in Fig. 4g. Birkenes II (Norway), Irafoss (Iceland), Pallas Matorova (Finland) and Risoe (Denmark) all experienced roughly an event every two days, whilst only Leba (Poland), Preila (Lithuania) and Rucava (Latvia) did not experience any pollution episodes. In total, 283 pollution events are observed ~~across Europe~~ at 22 EMEP stations indicating that widespread sulphurous pollution occurred across Europe in the months following the eruption.

The likelihood of Holuhraun being a main source of pollution for the 283 events can be established qualitatively using the IASI retrieved and modelled SO_2 column load animations ~~in the Supplement (S1)~~ or more robustly using the~~a~~ trajectory ~~analysis~~ framework ~~as~~ outlined ~~described~~ in Sect. 2.4. Using the latter approach, the main source of pollution for 11~~84~~ (39.2~~65~~%) of the events can be~~be~~ attributed to Holuhraun emissions (see Fig. 4g for a station-by-station breakdown). ~~-~~Of the 22 EMEP stations experiencing a sulphurous pollution ~~event~~ episode between September and October 2014, 19 stations~~20~~ endured at least one event influenced by the eruption. Note that other sources of pollutants may ~~also~~ contribute to the mass concentrations observed at these 11~~84~~ events, yet these contributions are likely minor given ~~-~~the rural setting of EMEP stations and that Holuhraun is the dominant ~~predominate~~ sulphurous source in the region covering this period. ~~-~~None of the combined 17 events observed at Bredkälen (Sweden) and Tustervatn (Norway) are attributed to Holuhraun emissions which, given that the plume has been shown to pass this area (~~e.g.~~e.g. Grahn et al., 2015; Ialongo et al., 2015), suggests an inconsistency in the trajectory analysis. This inconsistency could be resolved by revising the heights the trajectories are released at, by incorporating additional meteorological datasets and/or trajectory models, or by using a more comprehensive trajectory framework (e.g. dispersion modelling). As assessing our trajectory framework is not the focus here, these inconsistencies have not been explored further. ~~The choice of the input meteorological dataset is shown to dominate the uncertainty in trajectory calculations with the choice of trajectory model playing a smaller role, although no combination of the two is found superior (Gebhart et~~

Formatted: Not Highlight

Formatted: Not Highlight

~~al., 2005) and so changing them is unlikely to improve the analysis here. Instead, the inconsistency could be resolved by amending the initialisation altitudes of the two stations.~~ Nevertheless, the trajectory analysis shows that Holuhraun brought about significantly elevated sulphurous surface mass concentrations across Europe in September and October 2014; ~~which is~~a testament to the sheer volume of SO_2 emitted into the region by the eruption.

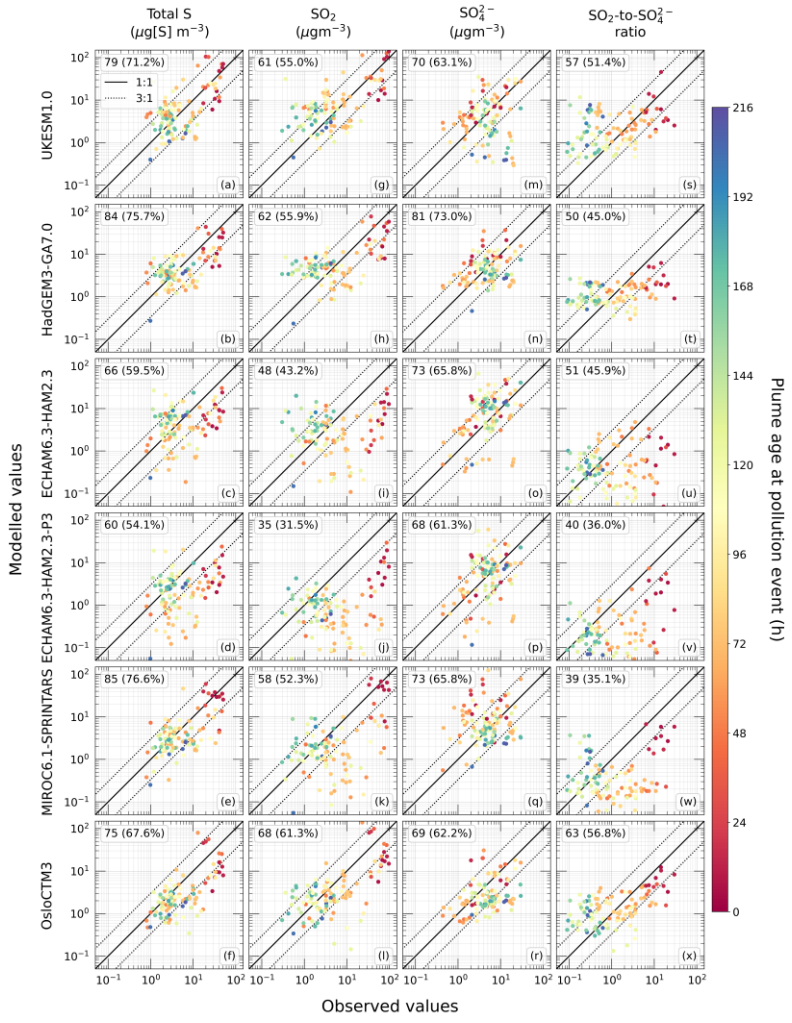
Total S
(μg[S] m^{-3})
SO_2
(μgm^{-3})
SO_4^{2-}
(μgm^{-3})
SO_2-to-SO_4^{2-}
ratio
UKESM1.0
HadGEM3-GA7.0
ECHAM6.3-HAM2.3
ECHAM6.3-HAM2.3-P3
MIROC6.1-SPRINTARS
OsloCTM3
79 (71.2%)
61 (55.0%)
70 (63.1%)
57 (51.4%)
84 (75.7%)
62 (55.9%)
81 (73.0%)
50 (45.0%)
66 (59.5%)
48 (43.2%)
73 (65.8%)
51 (45.9%)
60 (54.1%)
35 (31.5%)
68 (61.3%)
40 (36.0%)
85 (76.6%)
58 (52.3%)
73 (65.8%)
39 (35.1%)
75 (67.6%)
68 (61.3%)
69 (62.2%)
63 (56.8%)
1:1
3:1
Modelled values
Observed values
Plume age at pollution event (h)
216
192
168
144
120
96
72
48
24
0

555

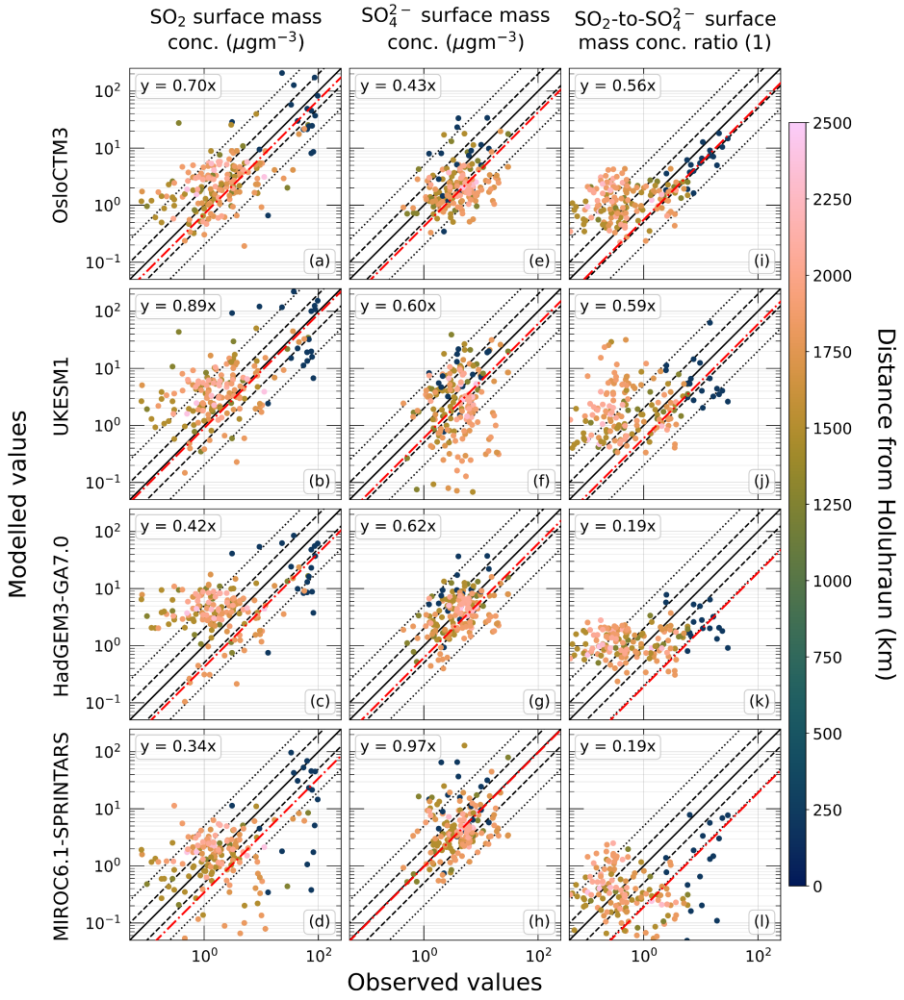

Figure 65: Modelled versus observed surface mass concentrations of total sulphur, SO_2 and SO_4^{2-}, and the SO_2-to-SO_4^{2-} ratio for 184 sulphurous pollution events attributed to Holuhraun emissions across 2 the2 EMEP networkstations for September and Octoberrom 1st September to 31st October 2014. Black lines from the inside out represent the 1:1, 2:1 and 5:1 boundaries,

Formatted: Left, Line spacing: single

~~whilst the red dashed lines represent the linear regression fit~~. Black solid and dashed lines represent parity and the 3-to-1 region respectively, with counts of points within the latter given. ~~Note that o~~Observational errors are too small to ~~be~~ discern~~ible~~.

Our catalogue of ~~volcanically influenced~~ 111 sulphurous pollution events attributed to Holuhraun emissions is used to assess model performance in capturing the surface level behaviour of the plume. Fig. ~~6~~5 displays~~shows~~ the modelled versus observed surface mass concentrations of total sulphur (a-f), SO_2 (~~a~~g-~~l, b, c, d~~), and ~~and~~ SO_4^{2-} (~~e, f, g, h~~m-r), and the SO_2-to-SO_4^{2-} ratio (~~i, j, k, l~~s-x) of ~~the 184 volcanic~~the volcanically influenced episodes with colouring used to highlight the plume age at the time of sampling. In terms of reproducing the observed total sulphur content, MIROC6.1-SPRINTARS, HadGEM3-GA7.0, and UKESM1.0 perform well with 76.6%, 75.7%, and 71.2% of values within the 3-to-1 range respectively, whilst the two ECHAM variants capture just below 60%. These lower values are largely due to underestimating the higher sulphur content observed in the young plume (0–96 h) which itself is due to a considerable underestimation of the underlying SO_2 during these early stages of the plume. The SO_2 surface concentrations are also underestimated in MIROC6.1-SPRINTARS, yet for a slightly more mature plume (72–120 h), whilst the opposite is evident in UKESM1.0 and HadGEM3-GA7.0, predominantly for plume ages exceeding 96 h. The overestimation of European surface SO_2 concentrations in UKESM1.0 has been noted previously (Hardacre et al., 2021), albeit over longer timescales. OsloCTM3 simulates the SO_2 well, showing no apparent overprediction or underprediction. All models depict the observed decrease in SO_2 concentration with increasing plume age.

With respect to SO_4^{2-}, all models improve on their SO_2 performance with each model having at least 61% of simulated concentrations within the 3-to-1 range. The models show no obvious overestimation or underestimation, aside from UKESM1.0 and MIROC6.1-SPTRINARS where concentrations for plume ages above and below 96 h are generally underpredicted and overpredicted respectively. This underprediction of surface SO_4^{2-} across Europe by UKESM1.0 has been stated previously (Hardacre et al., 2021; Mulcahy et al., 2020). In addition, the models struggle most in capturing the observed SO_2-to-SO_4^{2-} ratios with only OsloCTM3 and UKESM1.0 having more than 50% of simulated values within 3-to-1 of the observed. Broadly, all models, except for the ECHAM variants, simulate lower ratios than observed for the young plume (0–96 h) and higher ratios for the mature plume (144–216 h). The two ECHAM variants largely underestimate the observed ratio across all plume ages. There exists a notable underprediction in the ratio by MIROC6.1-SPTRINARS for plume ages roughly between 24 h and 48 h. Both the observed and modelled ratios decrease with increasing plume age suggesting that SO_2 oxidation to SO_4^{2-} is occurring within the observed and simulated plumes.

~~The observed SO_4^{2-} surface mass concentrations displayed in Fig. 5e-h show no clear correlation with distance from the eruption vent.~~ ~~events for OsloCTM3, UKESM1, HadGEM3-GA7.0 and MIROC6.1-SPRINTARS. The remaining models are found in the Supplement (S26). The performance of the models is summarised in Table 4. The ability of the models to capture the observed SO_2 concentrations varies. Whilst OsloCTM3 and UKESM1 perform best with regression lines close to parity and 83.7% and 71.7% of values within the 5:1 range respectively, the remaining models struggle, most notably the ECHAM6.3~~

Formatted: Subscript
Formatted: Subscript
Formatted: Subscript
Formatted: Subscript
Formatted: Subscript
Formatted: Subscript
Formatted: Superscript
Formatted: Subscript
Formatted: Superscript

configurations with both having less than 58% of values within the 5:1 range. Observed SO_2 concentrations decrease with increasing distance from the eruption. Aside from ECHAM6.3-HAM2.3-P3, the models tend to overestimate the observed SO_2 surface mass concentrations at stations distanced greater than 1300 km from Holuhraun. Interestingly, Schmidt et al. (2015) found that NAME simulations underestimate the observed SO_2 surface mass concentrations at four Irish air quality monitoring stations each distanced between 1400 km and 1450 km away from the eruption. However, neither the NAME model or those stations are explored in this study and so a direct comparison is not possible. In addition, all models tend to underestimate the higher SO_2 concentrations observed at stations closer to Holuhraun which, coupled with the SO_2 overestimation at stations further away, could suggest that the removal of tropospheric SO_2 in the models is too slow in the region following the eruption.

		UKESM1	HadGEM3-GA7.0	MIROC6.1-SPRINTARS	ECHAM6.3-HAM2.3-P3	ECHAM6.3-HAM2.3	OsloCTM3
Regression Coefficient	SO_2	0.89 ± 0.08	0.42 ± 0.04	0.34 ± 0.03	0.118 ± 0.009	0.16 ± 0.02	0.70 ± 0.07
	SO_4^{2-}	0.60 ± 0.06	0.62 ± 0.05	0.97 ± 0.13	0.82 ± 0.08	1.32 ± 0.11	0.43 ± 0.05
	SO_2-to-SO_4^{2-} Ratio	0.60 ± 0.11	0.19 ± 0.02	0.19 ± 0.02	0.091 ± 0.013	0.08 ± 0.02	0.56 ± 0.03
Values within 5:1	SO_2	132 (71.7%)	121 (65.8%)	129 (70.1%)	91 (49.5%)	105 (57.1%)	154 (83.7%)
	SO_4^{2-}	144 (78.3%)	173 (94.0%)	157 (85.3%)	158 (85.9%)	156 (84.8%)	152 (82.6%)
	SO_2-to-SO_4^{2-} Ratio	96 (52.2%)	109 (59.2%)	100 (54.3%)	101 (54.9%)	114 (62.0%)	121 (65.8%)

Table 4: Summary of the modelled versus observed surface mass concentration behaviour of the 184 sulphurous pollution events attributed to Holuhraun emissions.

The observed SO_4^{2-} surface mass concentrations displayed in Fig. 5e-h show no clear correlation with distance from the eruption vent. Relative to their SO_2 regression lines, OsloCTM3 and UKESM1 perform poorer in replicating SO_4^{2-} surface mass concentrations whilst the remaining model performances improve, particularly MIROC6.1-SPRINTARS with a slope of 0.97 ± 0.13 and HadGEM3-GA7.0 where 94.0% of modelled concentrations lie within the 5:1 range. There is no apparent overestimation or underestimation of SO_4^{2-} concentrations across the models, aside from perhaps in UKESM1 where underestimation occurs at some stations distanced greater than 1700 km from Holuhraun. The models struggle most in capturing the SO_2-to-SO_4^{2-} ratio shown in Fig. 5i-l as only UKESM1 and OsloCTM3 show modelled regression slopes above 0.55. Although this poor performance relative to the simulation of the individual SO_2 and SO_4^{2-} concentrations is somewhat expected as the models are essentially trying to correctly capture the behaviour of two pollutants as opposed to one. Observed and modelled ratios become smaller with increasing distance from the volcanic vent suggesting that SO_2 oxidation to SO_4^{2-} is occurring within the observed and simulated plumes.

Possible causes of differences between observed and simulated surface level behaviour of far afield Holuhraun pollutants, such as vertical resolution, source emission profile, and sub grid turbulence parameterisations, have been explored in depth previously (e.g. Boichu et al., 2016; Schmidt et al., 2015) and so will not be explored further here. As t~~T~~hese challenges are not specific to Holuhraun and feature extensively in most numerical dispersion problems, the ~~and so~~ discrepancies that arise from them should not ~~act as evidence that~~ act as evidence against the use of these models for the ACI investigation in ~~a model is not fit to be used in~~ Part 2 of this study. In fact, given the relatively fine spatial and temporal resolution that these coarse models are being assessed against here, they perform commendably in capturing the surface level behaviour of the plume.

Formatted: Justified, None, Space Before: 0 pt, After: 0 Don't keep with next

Formatted: Justified, None, Space Before: 0 pt, After: 0 Don't keep with next

Formatted: Justified, None, Space Before: 0 pt, After: 0 Don't keep with next

Formatted: Highlight

6~~5 Rate of~~ In-Plume SO_2 oxidation to SO_4^{2-}

We have demonstrated that Holuhraun emissions affected the troposphere over long distances triggering SO_2 and SO_4^{2-} pollution events across Europe and that the ratio of SO_2-to-SO_4^{2-} observed during these episodes decreases as the plume ages. This suggests that SO_2 oxidation to SO_4^{2-} is occurring as the plume matures. There are two main pathways for this conversion in the troposphere:

~~The pathways of SO_2 oxidation to SO_4^{2-} are essentially through~~ gas-phase reactions, largely with the hydroxyl radical (OH-), ~~(slower)~~ and aqueous-phase ~~(faster)~~ reactions with dissolved ozone (O_3) and ~~with the hydroxyl radical (OH^-) and~~ hydrogen peroxide (H_2O_2) ~~respectively~~ (e.g. Calvert et al., 1978; Stevenson et al., 2003). The ratio of SO_2-to-SO_4^{2-} is therefore useful in assessing whether oxidation processes are being accurately represented in the models; a ratio greater than that observed suggests that the overall ~~one or both~~ oxidation processes are too slow whilst a ratio less than that observed suggests that the overall ~~one or both~~ oxidation processes are too fast. This assessment is carried out here using ~~By using the ratio of the two pollutants, the variation in the absolute Holuhraun daily sulphurous emission flux can be ignored. Here the SO_2 oxidation to SO_4^{2-} is explored using~~ the 111 ~~our catalogue of~~ pollution events attributed to Holuhraun emissions ~~across the 22 EMEP stations~~. By focusing on ~~For each event, the trajectory analysis used previously to verify volcanic influence is now used to estimate the transport time of the plume to the station, essentially the plume age, following the method outlined in Sect. 2.4~~the ratio of the two pollutants as opposed to the total sulphur content and assuming that volcanic SO_2 and SO_4^{2-} coexist, the ~~.~~variation in the absolute Holuhraun daily sulphurous emission flux can be ignored

Formatted: Subscript
Formatted: Subscript
Formatted: Superscript
Formatted: Normal
Formatted: Subscript

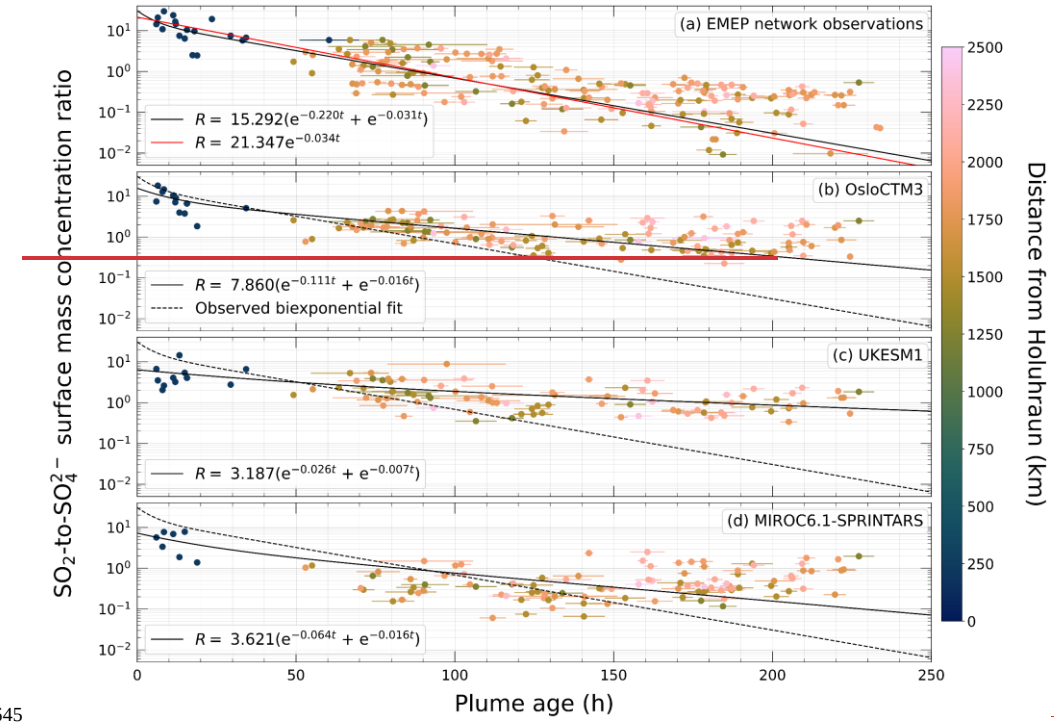

~~**Figure 6:** (a) Observed and (b-d) modelled SO_2-to-SO_4^{2-} surface mass concentration ratios of sulphurous pollution events attributed to Holuhraun emissions with respect to the plume age (see Sect. 2.4). Red and black solid lines represent monoexponential and biexponential fits respectively. Black dashed lines represent the observed biexponential fit overlayed on the model simulation subplots. Note the observed ratio errors are too small to be discernible.~~

Fig. ~~7~~6a shows the observed surface mass concentration ratio of SO_2-to-SO_4^{2-} on a logarithmic scale of the 111 sulphurous pollution events attributed to Holuhraun emissions ~~for the 184 events~~ versus the age of the plume at the time of sampling, with colouring highlighting the plume's travel distance from the eruption. A variety of plume ages and SO_2-to-SO_4^{2-} ratios make it apparent that ~~(Sect. 2.4). A variety of plume ages are estimated ranging from 6 h to 234 h with the plume associated with events observed at stations closer to Holuhraun generally being younger than events observed further away. Such a considerable difference in the estimated parcel age, coupled with a large range in observed ratios (0.01 to 29.75) likely means~~

~~that the local volcanic pollution sampled across the 22 EMEP stations stems from~~ the plume is sampled during different stages of ~~its lifetime~~maturity~~. It is worth noting that even some individual stations experience the plume at notably varying ages such as Utö (Finland) where events are associated with the plume aged between 96 h to 210 h. Similarly, the observed SO_2-to-SO_4^{2-} ratio varies up to an order of magnitude for the plume at comparable ages. This variability is visible in the apparent vertical spread of the data in Fig. 6a. For example, plume ages between 70 h to 80 h have SO_2-to-SO_4^{2-} ratios between 0.5 and 5.9~~. The linear characteristics of Fig. 7a, along with the curve depicted in the equivalent linear scale figure in the Supplement (S28), imply an exponential decay of the SO_2-to-SO_4^{2-} ratio with plume age; a relationship commonly associated with the depletion of volcanic SO_2 and one that assumes first order kinetics with respect to the SO_2 concentrations (e.g. Ilyinskaya et al., 2021; McGonigle et al., 2004; Oppenheimer et al., 1998; Pattantyus et al., 2018). Consequently, here we fit the observed data to an exponential decay function using non-linear total least squares regression as this considers both the ratio and plume age uncertainties. The derived SO_2-to-SO_4^{2-} oxidation rate constant is 0.032 ± 0.002 h^{-1} corresponding to an *e*-folding time of 1.30 ± 0.08 days. Using IASI retrieved SO_2 column loads, Carboni et al. (2019a) estimate Holuhraun SO_2 depletion as having a mean 6-month *e*-folding time of 2.4 ± 0.6 days, whilst Schmidt et al. (2015) derive a mean September SO_2 *e*-folding time of 2.0 ± 0.8 days using NAME simulations of the eruption. Whilst not directly comparable, as these studies have not estimated the oxidation rate explicitly and focus on different time periods, both estimates are of similar magnitude to the SO_2 oxidation *e*-folding time found here. Assuming our exponential decay relationship holds close to the eruption vent, this study estimates a near-vent SO_2-to-SO_4^{2-} ratio of 25 ± 5. This result agrees with Ilyinskaya et al. (2017) who report SO_2-to-SO_4^{2-} ratios of 2 to 250 and 4 to 94 at 100 km and 250 km from the vent respectively. Boichu et al. (2019) estimate a slightly lower near-vent SO_2-to-SO_4^{2-} ratio of 19.7 using a linear model created from 5 observations to describe the evolution of the SO_2-to-SO_4^{2-} ratio.

Formatted: Subscript
Formatted: Subscript
Formatted: Superscript
Formatted: Font: Italic
Formatted: Subscript

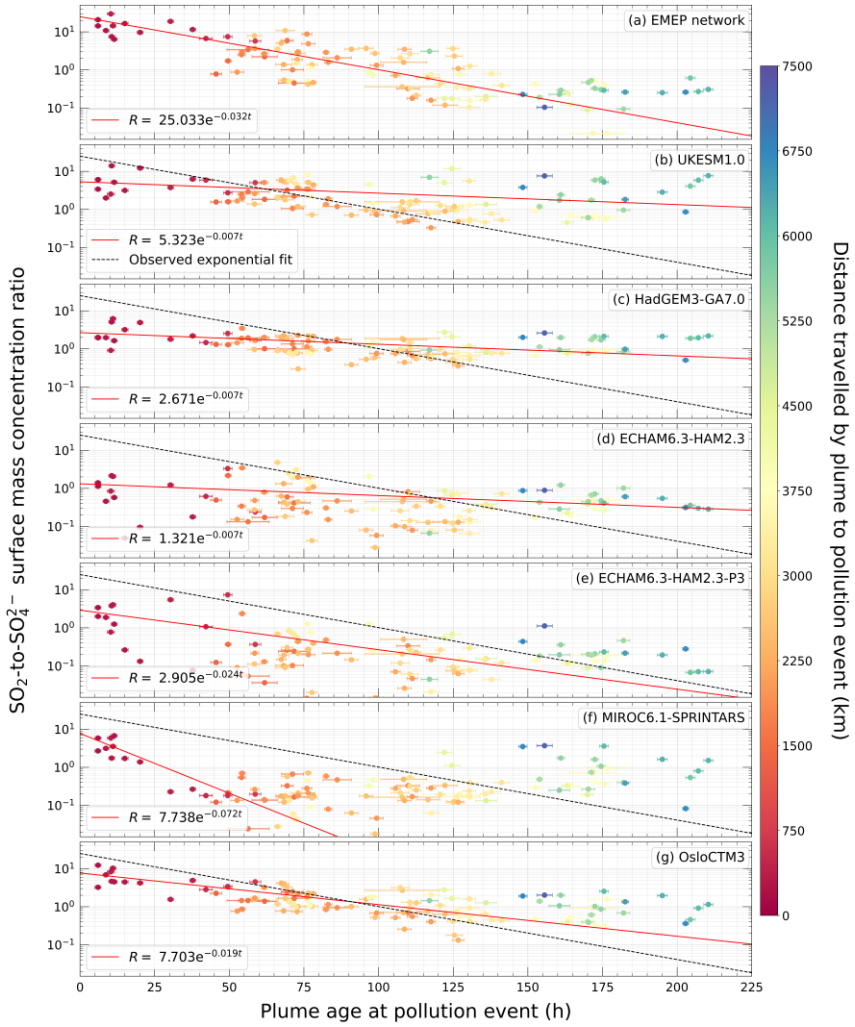

~~. Both these variations noted at individual stations and within the plume at similar ages is testament to the complexity of SO_2 oxidation to SO_4^{2-} within volcanic plumes and may be related to the relative contribution of the gas-phase and aqueous-phase pathways, although oxidant limitation (i.e. the SO_2 concentrations may be so high that OH^- and/or H_2O_2 are reduced to such an extent that the reactions cease to occur) may also play a key role as it has been shown for the Kīlauea volcano, Hawaii~~

(Pattantyus et al., 2018). **Figure 76:** (a) Observed and (b-gd) modelled SO_2-to-SO_4^{2-} surface mass concentration ratios of sulphurous pollution events attributed to Holuhraun emissions with respect to the plume age at the time of sampling (see Sect. 2.4for September and October 2014). Red lines and black solid lines represent the monoexponential and biexponentialdecay fits respectively. Black dashed lines representare the observed exponential biexponential fit overlayed onto the modelled ratio simulation subplots. Note the observed ratioObservational errors are too small to be discernible.:

Table 4: Summary of the observed and modelled in-plume SO_2 oxidation to SO_4^{2-} using the sulphurous pollution events attributed to Holuhraun emissions for September and October 2014. Note that ECHAM6.3-HAM2.3 cannot be described sufficiently by a biexponential function and so the oxidation rate and *e*-folding time here relate to the overall oxidation and are derived from a monoexponential function (i.e. one decay component only).

	EMEP network	UKESM1.0	HadGEM3-GA7.0	MIROC6.1-SPRINTARS	ECHAM6.3-HAM2.3-P3	ECHAM6.3-HAM2.3	OsloCTM3
Near-vent SO_2-to-SO_4^{2-} ratio	25 ± 5	5.3 ± 0.8	2.7 ± 0.3	7.7 ± 1.5	2.9 ± 0.5	1.3 ± 0.2	7.7 ± 0.6
SO_2 oxidation rate constant (h^{-1})	0.032 ± 0.002	0.0069 ± 0.0018	0.0070 ± 0.0012	0.072 ± 0.018	0.024 ± 0.004	0.007 ± 0.002	0.0191 ± 0.0016
SO_2 oxidation *e*-folding time (days)	1.30 ± 0.08	6.0 ± 1.6	5.9 ± 1.0	0.58 ± 0.15	1.7 ± 0.3	5.8 ± 1.8	2.18 ± 0.18

Table 5: Summary of the observed and modelled in-plume SO_2 oxidation to SO_4^{2-} using the sulphurous pollution events attributed to Holuhraun emissions. Note that ECHAM6.3-HAM2.3 cannot be described sufficiently by a biexponential function and so the oxidation rate and *e*-folding time here relate to the overall oxidation and are derived from a monoexponential function (i.e. one decay component only).

The linear characteristics of Fig. 6a hint at an observed exponential decay between the SO_2-to-SO_4^{2-} ratio and plume age. This relationship is clearer in the equivalent linear scale figure contained in the Supplement (S28). The observed data is fitted to monoexponential and biexponential functions. A biexponential function, a sum of two individual exponential decay components, is chosen to assess the feasibility in distinguishing between the decay caused by gas-phase and aqueous-phase oxidation. Both functions are fitted using non-linear total least squares regression which considers both the ratio and plume age uncertainties. The biexponential function better captures the observations and so will be the focus here. The observed biexponential decay components suggest a gas-phase SO_2 oxidation rate of 0.031 ± 0.002 h^{-1} and an aqueous-phase SO_2

~~oxidation rate of 0.22 ± 0.16 h^{-1} corresponding to *e*-folding times of 1.34 ± 0.07 days and 0.19 ± 0.14 days respectively. Using IASI retrieved SO_2 column loads, Carboni et al. (2019) estimate Holuhraun having a mean 6-month SO_2 *e*-folding time of 2.4 ± 0.6 days whilst Schmidt et al. (2015) derive a mean September SO_2 *e*-folding time of 2.0 ± 0.8 days using NAME simulations of the eruption. Whilst not directly comparable, as these studies have not treated the two oxidation pathways individually and focus on different time periods, both estimates are consistent with the gas-phase SO_2 *e*-folding time found here. Assuming the biexponential decay relationship holds close to the eruption vent, this study estimates a near-vent ratio of 31 ± 4. This result agrees with Ilyinskaya et al. (2017) where SO_2-to-SO_4^{2-} ratios of 2 to 250 and 4 to 94 are observed at 100 km and 250 km from the vent respectively. Boichu et al. (2019) estimate a lower near-vent ratio of 19.7 using a similar method presented here, yet this study assumes the ratio evolves linearly and considers only 5 events with plume ages ranging from 50 h to 80 h.~~

Fig. 6b-~~gd show~~ depicts~~s~~ the modelled surface mass concentration ratio of SO_2-to-SO_4^{2-} versus the age of the plume that these ratios are sampled in. ~~imulated in for OsloCTM3, UKESM1 and MIROC6.1-SPRINTARS. The remaining models are found in the Supplement (S27-28).~~ All models display an exponential relationship between the SO_2-to-SO_4^{2-} and plume age, albeit not across the full time range in the case of MIROC6.1-SPRINTARS. Each~~Each~~ model is fitted to an ~~bi~~exponential decay function which is given by the solid red line with the observed fit overlayed in the black dashed line for comparison. Due to how our plume age error tends to increase with plume age, ratios sampled in the mature plume have less influence on the fitting than those sampled in the younger plume. ~~Of the 184 surface-level pollution events attributed to Holuhraun emissions, only those deemed to have been successfully captured by a model are used for each fit. A modelled event is considered successful if both the surface mass concentrations of SO_2 and SO_4^{2-} are within a 5:1 range of that observed. There is no requirement on the value of the modelled SO_2-to-SO_4^{2-} ratio.~~ The ~~n~~exponential decay ~~umber of successfully modelled events and the biexponential~~ parameter estimates for ~~all~~ the models are displayed in Table ~~4~~5. The modelled near-vent ratios are all smaller than that derived from observations, yet ~~all~~ still agree with those found in~~by~~ Ilyinskaya et al. (2017). Except for MIROC6.1-SPRINTARS, ~~A~~ all model derived ~~gas-phase~~ oxidation rate~~ss~~ are slower than that derived from observations, ranging from being roughly just under twice as slow in ECHAM6.3-HAM2.3-P3 and OsloCTM3, to 4.5 times as slow in UKESM1.0, HadGEM3-GA7.0, and ECHAM6.3-HAM2.3. The seemingly poor fit of MIROC6.1-SPRINTARS is likely due to the underestimation of the ratios between 24 h and 48 h (see Sect. 5). If ratios across this time range were better represented, a slower oxidation rate constant in keeping with the other models could be expected resulting in a fit that better capture the ratios modelled in the more mature plume. Interestingly, there is no apparent correlation between a model's vertical resolution and a model's ability to capture the in-plume SO_2-to-SO_4^{2-} oxidation.

roughly being twice as slow in OsloCTM3 and MIROC6.1-SPRINTARS, to up to 10 times as slow in HadGEM3-GA7.0. Better agreement is found with the derived aqueous-phase oxidation rates with OsloCTM3, MIROC6.1-SPRINTARS and HadGEM3-GA7.0 in agreement with the observation derived value. However, the derived aqueous-phase oxidation rate in UKESM1 and ECHAM6.3-HAM2.3-P3 are slower than observed. Note that ECHAM6.3-HAM2.3 cannot be described sufficiently by a biexponential function and so the oxidation rate and *e*-folding time here relate to the overall oxidation and are derived from a monoexponential function (i.e. one decay component only) preventing a direct comparison with the derived observed values.

	Observations	UKESM1	HadGEM3-GA7.0	MIROC6.1-SPRINTARS	ECHAM6.3-HAM2.3-P3	ECHAM6.3-HAM2.3*	OsloCTM3
Events (Successfully Modelled)	184 (-)	99 (53.8%)	115 (62.5%)	108 (58.7%)	86 (46.7%)	89 (48.4%)	130 (70.7%)
Near-Vent SO_2-to-SO_4^{2-} Ratio	31 ± 4	6.4 ± 0.7	3.9 ± 0.6	7.2 ± 1.4	2.7 ± 0.3	2.2 ± 0.4	16 ± 3
Aqueous Oxidation Rate (h^{-1})	0.22 ± 0.16	0.03 ± 0.02	0.04 ± 0.03	0.06 ± 0.07	0.02 ± 0.02	0.010 ± 0.002	0.11 ± 0.09
Aqueous *e*-folding Time (days)	0.19 ± 0.14	1.6 ± 1.0	1.1 ± 1.0	0.7 ± 0.7	2 ± 2	4.2 ± 0.8	0.4 ± 0.3
Gaseous Oxidation Rate (h^{-1})	0.031 ± 0.002	0.007 ± 0.002	0.003 ± 0.001	0.016 ± 0.002	0.007 ± 0.002	-	0.016 ± 0.003
Gaseous *e*-folding Time (days)	1.34 ± 0.07	6.3 ± 1.4	13 ± 5	2.6 ± 0.4	6 ± 2	-	2.7 ± 0.4

Formatted Table

Table 5: Summary of the observed and modelled in-plume SO_2 oxidation to SO_4^{2-} using the sulphurous pollution events attributed to Holuhraun emissions. Note that ECHAM6.3-HAM2.3 cannot be described sufficiently by a biexponential function and so the oxidation rate and *e*-folding time here relate to the overall oxidation and are derived from a monoexponential function (i.e. one decay component only).

7~~5~~ Summary and Conclusions

By releasing 9.6–11.8 Mt of SO_2 into the lower troposphere across nearly 6 months, the 2014–2015 Holuhraun eruption offers an opportunity to challenge the capability of GCMs in capturing the characteristics of tropospheric sulphate aerosol intricacies resulting from effusive eruptions and assess the potential impact of subsequent aerosol-cloud interactions. A model inter-comparison effort has been initiated to leverage this opportunity and the results from Part 1 of the two-part analysis are presented here. Remote sensing data of SO_2, and surface level SO_2 and SO_4^{2-} mass concentration measurements are used in conjunction with trajectory modelling to evaluate the performance of 5 GCMs and a CTM in simulating the spatial and chemical evolution of the SO_2 plume across the North Atlantic and Europe.

A comparison against IASI SO_2 retrievals show~~s~~ that the models capture the evolution of the volcanic plume within the surrounding region well during September and October 2014. Holuhraun emissions are the dominant source of SO_2 in the models and the spatial transport of the associated SO_2 plume is well replicated. The ~~vertical distribution of the~~ SO_2 plume height is slightly ~~underestimated~~ overestimated by the models, whereas there is no general overestimation or underestimation in simulating the SO_2 mass burdens; it is model dependent. The temporal variability of both these plume characteristics is well captured. Discrepancies with the IASI retrievals could be due to several factors including the limitations of the IASI retrievals (e.g. Carboni et al., 2019a), and discrepancies between the idealised volcanic emission profile used by the models and the real emissions (e.g. Steensen et al., 2016). A comparison against retrievals of volcanic SO_2 from other satellite instrumentations may yield different conclusions, yet the descriptions of the plume spatial distribution made with other remote sensing products are similar (e.g. OMI: Ialongo et al., 2015; Schmidt et al., 2015, Steensen et al., 2016; OMPS-NN: Ialongo et al., 2015; GOME-2: Twigg et al., 2016). Even though the model spatial representations of the eruption are not perfect, our~~the~~ intent here ~~here~~ is rather to identify~~assess~~ the variations in the models' ~~SO_4^{2-}~~ transport ~~production~~ of Holuhraun SO_2 ~~in the different models whilst considering everything else equal (i.e. same emissions)~~ as this ~~understanding the aerosol perturbation~~ will help discern the impact on cloud properties and assess the ACIs in Part 2.

Formatted: Not Highlight

By combining the surface mass concentration measurements of SO_2 and SO_4^{2-} made during September and October 2014 across the EMEP network with single-particle trajectories calculated using the HYSPLIT model, the simulated surface level behaviour of the plume was assessed. Of the 283 sulphurous pollution events identified, ~~184~~ 111 are attributed to Holuhraun emissions. Generally, the models reproduce the measured elevated surface level concentrations during these volcanically influenced events, yet they struggle in simulating the correct magnitude, notably the ratio of SO_2-to-SO_4^{2-} ~~SO_2~~ which is often underestimated and overestimated for the young and mature plume respectively. Although this should not be discouraging as~~,~~ ~~as noted in Boichu et al. (2016),~~ capturing volcanic sulphurous pollutant surface mass concentrations far afield at a specific location and time is challenging even for CTMs ~~with~~ of finer ~~resolutions~~scales. We note that the models with finer vertical

resolutions, UKESM1.0, HadGEM3-GA7.0, and OsloCMT3, describe ground-level concentrations of Holuhraun pollution episodes best; a feature that has been noted previously by Boichu et al. (2016). Given the relatively coarse scale of the simulations discussed here, the surface level performance of the models is admirable.

Both the observed and modelled ratios of SO_2-to-SO_4^{2-} surface mass concentrations sampled within the plume are shown to decrease with increasing time and station distance from the eruption vent suggesting SO_2 oxidation to SO_4^{2-} is occurring. To explore this further, the ratios as a function of plume age have been analysed revealing an exponential decay. By fitting this decay to an biexponential function, the gas-phase and aqueous-phaseobserved and modelled oxidation rate constants for the volcanic SO_2 oxidation are estimated pathways can be estimated with their rates represented by the biexponential decay components. All models side from MIROC6.1-SPRINTARS, the in-plume SO_2-to-SO_4^{2-} oxidation is shown to be slower in the models than observed. This implies that the volcanic SO_2 introduced into the simulations may not be chemically converted fast enough relative to what is derived from surface measurements (if deposition effects are ignored). The considerable underestimation of the ratios sampled at plume ages between 24 h and 48 h is the suggested reasoning for MIROC6.1-SPRINTARS exhibiting opposing behaviour. No correlation between a model's vertical resolution and a model's derived SO_2 oxidation rate is found.aside from ECHAM6.3-HAM2.3 benefit from the use of a biexponential fit to describe the SO_2 decay suggesting that they replicate two oxidation pathways within the plume. The modelled derived aqueous-phase oxidation rates are in better agreement than the gas-phase oxidation rates with the observation derived values, yet altogether the oxidation in the modelled plumes are found to occur too slowly. This indicates that the volcanic SO_2 introduced into the simulations may not be chemically converted fast enough relative to what is derived from surface measurements. This study acknowledges that substantial assumptions are required to draw these conclusions, such as ignoring the effect of deposition.

The oxidation rate constants explored here are generalised values representing both the gas-phase and aqueous-phase pathways. This study attempted to help elucidate the complexity of volcanic SO_2 oxidation by fitting the SO_2-to-SO_4^{2-} ratios to a biexponential function, a sum of two individual exponential decay components, to distinguish between the two pathways by estimating individual gaseous and aqueous oxidation rate constants. Despite the success of previous studies in estimating and applying multiple rate constants to the describe the depletion of volcanic SO_2 (Ilyinskaya et al., 2021; Pattantyus et al., 2018), this study found no significant improvement in the fitting function versus a standard exponential decay (one exponential decay component). Categorising the SO_2-to-SO_4^{2-} ratios in terms of the conditions the air parcels are subject to during transport, such as time spent in-cloud, relative humidity, cloud pH, oxidant concentrations, time of day, and deposition rates, could reveal the dominant oxidation pathway/s affecting a particular group. The subsequent fitting versus plume age would then provide rate constant estimates of the mechanism/s in play. However, such a method would likely require a sophisticated Lagrangian framework, and it is beyond the scope of this work to explore the intricate chemical kinetics of volcanic SO_2 oxidation.

Formatted: Subscript

Formatted: Subscript

Formatted: Subscript

Overall, the 6 models considered here provide reasonable simulations of the spatial and chemical evolution of the Holuhraun plume and are considered competent enough to be used to explore the impacts of the eruption on ACIs (see Part 2 of this study). It is important to acknowledge, and is possibly relevant to the wider ACI community, that this analysis has also highlighted that the models do not perfectly capture the secondary SO_4^{2-} aerosol production during a large degassing event which may contribute to disagreements between model ACIs estimates due to differing underlying perturbations. We hope that our application of in situ sulphurous surface measurements to assess numerical models help bolster the case to retain and extend air monitoring networks of volcanic pollutants for use in future studies.

Code Availability

Code is available from the corresponding author on reasonable request.

Data Availability

The IASI SO_2 retrieval dataset is available on the CEDA Archive, https://catalogue.ceda.ac.uk/uuid/d40bf62899014582a72d24154a94d8e2 (Carboni et al., 2019b). The EMEP network surface SO_2 and SO_4^{2-} mass concentrations are available through the EBAS database, https://ebas.nilu.no/data-access/. All model data, including trajectory output, used in this study is available on Zenodo, https://doi.org/10.5281/zenodo.10160538~~/10.5281/zenodo.7786775~~ (Jordan, 2023).

Field Code Changed

Author Contributions

GJ, JH, and FM designed the experiment. GJ handled the remote sensing data and in situ surface measurements whilst GJ, DW-P, TT, DN, GM, and RS ran the model simulations. PK, ~~and~~ DGP, and ED provided HYSPLIT trajectories and offered guidance in their use. GJ, JH, FM, YC, AP, ED, and DGP analysed the spatial and chemical evolution of the Holuhraun plume. GJ prepared the manuscript with contributions from all co-authors.

Competing Interest

At least one of the (co-)authors is a member of the editorial board of Atmospheric Chemistry and Physics. The peer-review process was guided by an independent editor, and the authors also have no other competing interests to declare.

Acknowledgements

GJ and JH were funded under the European Union's Horizon 2020 research and innovation programme under the CONSTRAIN grant agreement 820829. GJ, JH, and FM are supported by the Met Office Hadley Centre Climate Programme funded by ~~BEIS~~DSIT. JH, YC, and AP would like to acknowledge funding from the NERC ADVANCE grant (NE/S015671/1). DGP would like to express his gratitude to Dr. Zak Kipling for providing support in obtaining HYSPLIT input files from ERA-Interim reanalysis data.

~~This study uses colour scales from Crameri (2018) to improve the accessibility of the figures for readers with colour-vision deficiencies.~~

References

Aas, W., Mortier, A., Bowersox, V., Cherian, R., Faluvegi, G., Fagerli, H., Hand, J., Klimont, Z., Galy-Lacaux, C., Lehmann, C. and Myhre, C.L.: Global and regional trends of atmospheric sulfur. Scientific reports, 9, 953, doi:10.1038/s41598-018-37304-0, 2019.

Ágústsdóttir, T., Woods, J., Greenfield, T., Green, R. G., White, R. S., Winder, T., Brandsdóttir, B., Steinthórsson, S., and Soosalu, H.: Strike-slip faulting during the 2014 Bárðarbunga-Holuhraun dike intrusion, central Iceland, Geophys. Res. Lett., 43, 1495– 1503, doi:10.1002/2015GL067423, 2016.

Arason, Þ., Bjornsson, H., Petersen, G. N., Jónasdóttir, E. B., and Oddsson B. B.: Plume height during the 2014–2015 Holuhraun volcanic eruption, Geophys. Res., Abstracts, EGU2015-11498, 2015.

Athanassiadou, M., Francis, P. N., Saunders, R. W., Atkinson, N. C., Hort, M. C., Havemann, S., Thelen, J.-C. and Bush, M.: A case study of sulphur dioxide identification in three different volcanic eruptions, using Infrared satellite observations (IASI), Met. Apps., 23, 477-490, doi: 10.1002/met.1572, 2016.

Barsotti, S.: Probabilistic hazard maps for operational use: the case of SO_2 air pollution during the Holuhraun eruption (Bárðarbunga, Iceland) in 2014–2015, Bull. Volcanol., 82, 56, doi:10.1007/s00445-020-01395-3, 2020.

Barsotti, S., Oddsson, B., Gudmundssonc, M. T., Pfeffer, M. A., Parks, M. M., Ófeigsson, B. G., Sigmundsson, F., Reynisson, V., Jónsdóttir, K., Roberts, M. J., Heiðarsson, E. P., Jónasdóttir, E. B., Einarsson, P., Jóhannsson, T., Gylfason, Á. G., and Vogfjörd, K.: Operational response and hazards assessment during the 2014–2015 volcanic crisis at Bárðarbunga volcano and associated eruption at Holuhraun, Iceland, J. Volcanol. Geotherm., 390, 106753, doi:10.1016/j.jvolgeores.2019.106753, 2020.

Berntsen, T., and Isaksen, I. S. A.: A global 3-D chemical transport model for the troposphere, 1, Model description and CO and Ozone results, J. Geophys. Res., 102(D17), 21239-21280, doi:10.1029/97JD01140, 1997.

Boichu, M., Favez, O., Riffault, V., Petit, J.-E., Zhang, Y., Brogniez, C., Sciare, J., Chiapello, I., Clarisse, L., Zhang, S., Pujol-Söhne, N., Tison, E., Delbarre, H., and Goloub, P.: Large-scale particulate air pollution and chemical fingerprint of volcanic sulfate aerosols from the 2014–2015 Holuhraun flood lava eruption of Bárðarbunga volcano (Iceland), Atmos. Chem. Phys., 19, 14253–14287, doi:10.5194/acp-19-14253-2019, 2019.

Boichu, M., Chiapello, I., Brogniez, C., Péré, J.-C., Thieuleux, F., Torres, B., Blarel, L., Mortier, A., Podvin, T., Goloub, P., Söhne, N., Clarisse, L., Bauduin, S., Hendrick, F., Theys, N., Van Roozendael, M., and Tanré, D.: Current challenges in modelling far-range air pollution induced by the 2014–2015 Bárðarbunga fissure eruption (Iceland), Atmos. Chem. Phys., 16, 10831–10845, doi:10.5194/acp-16-10831-2016, 2016.

~~Boichu, M., Favez, O., Riffault, V., Petit, J.-E., Zhang, Y., Brogniez, C., Sciare, J., Chiapello, I., Clarisse, L., Zhang, S., Pujol-Söhne, N., Tison, E., Delbarre, H., and Goloub, P.: Large-scale particulate air pollution and chemical fingerprint of volcanic sulfate aerosols from the 2014–2015 Holuhraun flood lava eruption of Bárðarbunga volcano (Iceland), Atmos. Chem. Phys., 19, 14253–14287, doi:10.5194/acp-19-14253-2019, 2019.~~

Formatted: Line spacing: Multiple 1.07 li

Breen, K. H., Barahona, D., Yuan, T., Bian, H., and James, S. C.: Effect of volcanic emissions on clouds during the 2008 and 2018 Kilauea degassing events, Atmos. Chem. Phys., 21, 7749–7771, doi:10.5194/acp-21-7749-2021, 2021.

Calvert, J.G., Bottenheim, J.W. and Strausz, O.P.: Mechanism of the homogeneous oxidation of sulfur dioxide in the troposphere, Atmos. Environ., 12, 197-226, doi:10.1016/0004-6981(78)90201-9, 1978.

Carboni, E., Grainger, R., Walker, J., Dudhia, A., and Siddans, R.: A new scheme for sulphur dioxide retrieval from IASI measurements: application to the Eyjafjallajökull eruption of April and May 2010, Atmos. Chem. Phys., 12, 11417–11434, doi:10.5194/acp-12-11417-2012, 2012.

Carboni, E., Grainger, R. G., Mather, T. A., Pyle, D. M., Thomas, G. E., Siddans, R., Smith, A. J. A., Dudhia, A., Koukouli, M. E., and Balis, D.: The vertical distribution of volcanic SO_2 plumes measured by IASI, Atmos. Chem. Phys., 16, 4343–4367, doi:10.5194/acp-16-4343-2016, 2016.

Carboni, E., Mather, T. A., Schmidt, A., Grainger, R. G., Pfeffer, M. A., Ialongo, I., and Theys, N.: Satellite-derived sulfur dioxide (SO_2) emissions from the 2014–2015 Holuhraun eruption (Iceland), Atmos. Chem. Phys., 19, 4851–4862, doi:10.5194/acp-19-4851-2019, 2019a.

Carboni, E., Taylor, I., and Grainger, D.: IASI retrieval of sulphur dioxide (SO_2) column amounts and altitude, 2014-09 to 2015-02, version 1.0. Centre for Environmental Data Analysis, https://catalogue.ceda.ac.uk/uuid/d40bf628999014582a72d24154a94d8e2, 2019b.

Carn, S. A., Yang, K., Prata, A. J., and Krotkov, N. A.: Extending the long-term record of volcanic SO_2 emissions with the Ozone Mapping and Profiler Suite nadir mapper, Geophys. Res. Lett., 42, 925– 932, doi:10.1002/2014GL062437, 2015.

Chen, Y., Haywood, J., Wang, Y., Malavelle, F., Jordan, G., Partridge, D., Fieldsend, J., De Leeuw, J., Schmidt, A., Cho, N., Oreopoulos, L., Platnick, S., Grosvenor, D., Field, P., and Lohmann, U.: Machine learning reveals climate forcing from aerosols is dominated by increased cloud cover, Nat. Geosci., 15, 609–614, doi:10.1038/s41561-022-00991-6, 2022.

Clarisse, L., Coheur, P. F., Prata, A. J., Hurtmans, D., Razavi, A., Phulpin, T., Hadji-Lazaro, J., and Clerbaux, C.: Tracking and quantifying volcanic SO_2 with IASI, the September 2007 eruption at Jebel at Tair, Atmos. Chem. Phys., 8, 7723–7734, doi:10.5194/acp-8-7723-2008, 2008

Clarisse, L., Hurtmans, D., Prata, A. J., Karagulian, F., Clerbaux, C., De Mazière, M., Coheur, P. F.: Retrieving radius, concentration, optical depth, and mass of different types of aerosols from high-resolution infrared nadir spectra, Appl. Opt., 49, 3713-3722, doi:10.1364/AO.49.003713, 2010.

~~Crameri, F.: Scientific colour maps, Zenodo, http://doi.org/10.5281/zenodo.1243862, 2018.~~

Dee, D. P., Uppala, S. M., Simmons, A. J., Berrisford, P., Poli, P., Kobayashi, S., Andrae, U., Balmaseda, M. A., Balsamo, G., Bauer, P., Bechtold, P., Beljaars, A. C. M., van de Berg, L., Bidlot, J., Bormann, N., Delsol, C., Dragani, R., Fuentes, M., Geer, A. J., Haimberger, L., Healy, S. B., Hersbach, H., Hólm, E. V., Isaksen, L., Kållberg, P., Köhler, M., Matricardi, M., McNally, A. P., Monge-Sanz, B. M., Morcrette, J.-J., Park, B.-K., Peubey, C., de Rosnay, P., Tavolato, C., Thépaut, J.-N. and Vitart, F.: The ERA-Interim reanalysis: configuration and performance of the data assimilation system, Q.J.R. Meteorol. Soc., 137, 553-597, doi:10.1002/qj.828, 2011.

Dietlicher, R., Neubauer, D., and Lohmann, U.: Prognostic parameterization of cloud ice with a single category in the aerosol-climate model ECHAM(v6.3.0)-HAM(v2.3), Geosci. Model Dev., 11, 1557–1576, doi:10.5194/gmd-11-1557-2018, 2018.

Formatted: Subscript

~~Dhomse, S. S., Emmerson, K. M., Mann, G. W., Bellouin, N., Carslaw, K. S., Chipperfield, M. P., Hommel, R., Abraham, N. L., Telford, P., Braesicke, P., Dalvi, M., Johnson, C. E., O'Connor, F., Morgenstern, O., Pyle, J. A., Deshler, T., Zawodny, J. M., and Thomason, L. W.: Aerosol microphysics simulations of the Mt.Pinatubo eruption with the UM-UKCA composition-climate model, Atmos. Chem. Phys., 14, 11221–11246, doi:10.5194/acp-14-11221-2014, 2014.~~Engström, A. and Magnusson, L.: Estimating trajectory uncertainties due to flow dependent errors in the atmospheric analysis, Atmos. Chem. Phys., 9, 8857–8867, doi:10.5194/acp-9-8857-2009, 2009.

Flower, V. J. B., and Kahn, R. A.: The evolution of Icelandic volcano emissions, as observed from space in the era of NASA's Earth Observing System (EOS), J. Geophys. Res. Atmos, 125, e2019JD031625, doi:10.1029/2019JD031625, 2020.

Gebhart, K. A., Schichtel, B. A., and Barna, M.G.: Directional biases in back trajectories caused by model and input data, J. Air Waste Manage., 55, 1649-1662, doi:10.1080/10473289.2005.10464758, 2005.

Gettelman, A., Schmidt, A., and Egill Kristjánsson, J.: Icelandic volcanic emissions and climate, Nature Geosci., 8, 243, doi:10.1038/ngeo2376, 2015.

Gíslason, S. R., Stefánsdóttir, G., Pfeffer, M. A., Barsotti, S., Jóhannsson, Th., Galeczka, I., Bali, E., Sigmarsson, O., Stefánsson, A., Keller, N. S., Sigurdsson, Á., Bergsson, B., Galle, B., Jacobo, V. C., Arellano, S., Aiuppa, A., Jónasdóttir, E. B., Eiríksdóttir, E. S., Jakobsson, S., Guðfinnsson, G. H., Halldórsson, S. A., Gunnarsson, H., Haddadi, B., Jónsdóttir, I., Thordarson, Th., Riishuus, M., Högnadóttir, Th., Dürig, T., Pedersen, G. B. M., Höskuldsson, Á., and Gudmundsson, M. T.: Environmental pressure from the 2014–15 eruption of Bárðarbunga volcano, Iceland, Geochem. Persp. Let. 1, 84-93, doi:10.7185/geochemlet.1509, 2015.

Grahn, H., von Schoenberg, P., and Brännström, N.: What's that smell? Hydrogen sulphide transport from Bardarbunga to Scandinavia, J. Volcanol. Geoth. Res., 303, 187–192, doi:10.1016/j.jvolgeores.2015.07.006, 2015.

Gudmundsson, A., Lecoeur, N., Mohajeri, N., and Thordarson, T.: Dike emplacement at Bardarbunga, Iceland, induces unusual stress changes, caldera deformation, and earthquakes, Bull. Volcanol., 76, 1-7, doi:10.1007/s00445-014-0869-8, 2014.

Haghighatnasab, M., Kretzschmar, J., Block, K., and Quaas, J.: Impact of Holuhraun volcano aerosols on clouds in cloud-system-resolving simulations, Atmos. Chem. Phys., 22, 8457–8472, doi:10.5194/acp-22-8457-2022, 2022.

Hardacre, C., Mulcahy, J. P., Pope, R. J., Jones, C. G., Rumbold, S. T., Li, C., Johnson, C., and Turnock, S. T.: Evaluation of SO_2, SO_4^{2-} and an updated SO_2 dry deposition parameterization in the United Kingdom Earth System Model, Atmos. Chem. Phys., 21, 18465–18497, doi:10.5194/acp-21-18465-2021, 2021.

Harris, J. M., Drexler, R. R., and Oltmans, S. J.: Trajectory model sensitivity to differences in input data and vertical transport method, J. Geophys. Res., 110, D14109, doi:10.1029/2004JD005750, 2005.

Haywood, J. M., Jones, A., Clarisse, L., Bourassa, A., Barnes, J., Telford, P., Bellouin, N., Boucher, O., Agnew, P., Clerbaux, C., Coheur, P., Degenstein, D., and Braesicke, P.: Observations of the eruption of the Sarychev volcano and simulations using the HadGEM2 climate model, J. Geophys. Res., 115, D21212, doi:10.1029/2010JD014447, 2010.

Heaviside, C., Witham, C., and Vardoulakis, S.: Potential health impacts from sulphur dioxide and sulphate exposure in the UK resulting from an Icelandic effusive volcanic eruption, Sci. Total Environ., 774, 145549, doi:10.1016/j.scitotenv.2021.145549, 2021.

Formatted: Subscript
Formatted: Subscript
Formatted: Superscript
Formatted: Subscript

Hughes, E. J., Sparling, L. C., Carn, S. A., and Krueger, A. J.: Using horizontal transport characteristics to infer an emission height time series of volcanic SO_2, J. Geophys. Res., 117, D18307, doi:10.1029/2012JD017957, 2012.

Ialongo, I., Hakkarainen, J., Kivi, R., Anttila, P., Krotkov, N. A., Yang, K., Li, C., Tukiainen, S., Hassinen, S., and Tamminen, J.: Comparison of operational satellite SO_2 products with ground-based observations in northern Finland during the Icelandic Holuhraun fissure eruption, Atmos. Meas. Tech., 8, 2279–2289, doi:10.5194/amt-8-2279-2015, 2015.

Ilyinskaya, E., Mason, E., Wieser, P. E., Holland, L., Liu, E. J., Mather, T. A., Edmonds, M., Whitty, R. C. W, Elias, T., Nadeau, P. A., Schneider, D., McQuaid, J., B., Allen, S. E., Harvey, J., Oppenheimer, C., Kern, C., and Damby, D.: Rapid metal pollutant deposition from the volcanic plume of Kīlauea, Hawai'I, Commun. Earth Environ., 2, 78, doi:10.1038/s43247-021-00146-2, 2021.

Ilyinskaya, E., Schmidt, A., Mather, T. A., Pope, F. D., Witham, C., Baxter, P., Jóhannsson, T., Pfeffer, M., Barsotti, S., Singh, A., Sanderson, P., Bergsson, B., Kilbride, B. M., Donovan, A., Peters, N., Oppenheimer, C., and Edmonds, M.: Understanding the environmental impacts of large fissure eruptions: Aerosol and gas emissions from the 2014–2015 Holuhraun eruption (Iceland), Earth Planet. Sci. Lett., 472. 309-322, doi:10.1016/j.epsl.2017.05.025, 2017.

Jordan, G.: Volcanic Aerosol-Cloud Interactions (VolcACI) Experiment: Part 1 Dataset, (v2), Zendo, doi:10.5281/zenodo.10160538~~https://doi.org/10.5281/zenodo.7786775~~, 2023.

Keller, N., Stefani, M., Einarsdóttir, S. R., Helgadóttir, Á. K., Helgason, R., Ásgeirsson, B. U., Helgadóttir, D., Helgadóttir, I. R., Tinganelli, L., Brink, S. H., Snorrason, A., and Þórsson, J.: National Inventory Report: Emissions of Greenhouse Gases in Iceland from 1990 to 2020, The Environment Agency of Iceland: Reykjavík, Iceland, 2022.

de Leeuw, J., Schmidt, A., Witham, C. S., Theys, N., Taylor, I. A., Grainger, R. G., Pope, R. J., Haywood, J., Osborne, M., and Kristiansen, N. I.: The 2019 Raikoke volcanic eruption – Part 1: Dispersion model simulations and satellite retrievals of volcanic sulfur dioxide, Atmos. Chem. Phys., 21, 10851–10879, doi:10.5194/acp-21-10851-2021, 2021.

Li, C., Krotkov, N. A., Carn, S., Zhang, Y., Spurr, R. J. D., and Joiner, J.: New-generation NASA Aura Ozone Monitoring Instrument (OMI) volcanic SO_2 dataset: algorithm description, initial results, and continuation with the Suomi-NPP Ozone Mapping and Profiler Suite (OMPS), Atmos. Meas. Tech., 10, 445–458, doi:10.5194/amt-10-445-2017, 2017.

Lund, M. T., Myhre, G., Haslerud, A. S., Skeie, R. B., Griesfeller, J., Platt, S. M., Kumar, R., Myhre, C. L., and Schulz, M.: Concentrations and radiative forcing of anthropogenic aerosols from 1750 to 2014 simulated with the Oslo CTM3 and CEDS emission inventory, Geosci. Model Dev., 11, 4909–4931, doi:10.5194/gmd-11-4909-2018, 2018.

Malavelle, F. F., Haywood, J. M., Jones, A., Gettelman, A., Clarisse, L., Bauduin, S., Allan, R. P., Karset, I. H. H., Kristjánsson, J. E., Oreopoulos, L., Cho, N., Lee, D., Bellouin, N., Boucher, O., Grosvenor, D. P., Carslaw, K. S., Dhomse, S., Mann, G. W., Schmidt, A., Coe, H., Hartley, M. E., Dalvi, M., Hill, A. A., Johnson, B. T., Johnson, C. E., Knight, J. R., O'Connor, F. M., Partridge, D. G., Stier, P., Myhre, G., Platnick, S., Stephens, G. L., Takahashi, H., and Thordarson, T.: Strong constraints on aerosol–cloud interactions from volcanic eruptions, Nature, 546, 485–491, doi:10.1038/nature22974, 2017.

Formatted: Subscript

Formatted: Subscript

Formatted: Not Highlight

McCoy, D. T., and Hartmann, D. L.: Observations of a substantial cloud–aerosol indirect effect during the 2014–2015 Bárðarbunga-Veiðivötn fissure eruption in Iceland, Geophys. Res. Lett., 42, 409–410,414, doi:10.1002/2015GL067070, 2015.

McGonigle, A. J. S., Delmelle, P., Oppenheimer, C., Tsanev, V. I., Delfosse, T., Williams-Jones, G., Horton, K., and Mather, T. A.: SO_2 depletion in tropospheric volcanic plumes, Geophys. Res. Lett., 31, L13201, doi:10.1029/2004GL019990, 2004.

~~Malavelle, F. F., Haywood, J. M., Jones, A., Gettelman, A., Clarisse, L., Bauduin, S., Allan, R. P., Karset, I. H. H., Kristjánsson, J. E., Oreopoulos, L., Cho, N., Lee, D., Bellouin, N., Boucher, O., Grosvenor, D. P., Carslaw, K. S., Dhomse, S., Mann, G. W., Schmidt, A., Coe, H., Hartley, M. E., Dalvi, M., Hill, A. A., Johnson, B. T., Johnson, C. E., Knight, J. R., O'Connor, F. M., Partridge, D. G., Stier, P., Myhre, G., Platnick, S., Stephens, G. L., Takahashi, H., and Thordarson, T.: Strong constraints on aerosol–cloud interactions from volcanic eruptions, Nature, 546, 485–491, doi:10.1038/nature22974, 2017.~~Mulcahy, J. P., Johnson, C., Jones, C. G., Povey, A. C., Scott, C. E., Sellar, A., Turnock, S. T., Woodhouse, M. T., Abraham, N. L., Andrews, M. B., Bellouin, N., Browse, J., Carslaw, K. S., Dalvi, M., Folberth, G. A., Glover, M., Grosvenor, D. P., Hardacre, C., Hill, R., Johnson, B., Jones, A., Kipling, Z., Mann, G., Mollard, J., O'Connor, F. M., Palmiéri, J., Reddington, C., Rumbold, S. T., Richardson, M., Schutgens, N. A. J., Stier, P., Stringer, M., Tang, Y., Walton, J., Woodward, S., and Yool, A.: Description and evaluation of aerosol in UKESM1 and HadGEM3-GC3.1 CMIP6 historical simulations, Geosci. Model Dev., 13, 6383–6423, doi:10.5194/gmd-13-6383-2020, 2020.

Neubauer, D., Ferrachat, S., Siegenthaler-Le Drian, C., Stier, P., Partridge, D. G., Tegen, I., Bey, I., Stanelle, T., Kokkola, H., and Lohmann, U.: The global aerosol–climate model ECHAM6.3–HAM2.3 – Part 2: Cloud evaluation, aerosol radiative forcing, and climate sensitivity, Geosci. Model Dev., 12, 3609–3639, doi:10.5194/gmd-12-3609-2019, 2019.

Nieminen, T., Yli-Juuti, T., Manninen, H. E., Petäjä, T., Kerminen, V.-M., and Kulmala, M.: Technical note: New particle formation event forecasts during PEGASOS–Zeppelin Northern mission 2013 in Hyytiälä, Finland, Atmos. Chem. Phys., 15, 12385–12396, doi:10.5194/acp-15-12385-2015, 2015.

NILU: EMEP manual for sampling and chemical analysis, Tech. rep., Norwegian Institute for Air Research, available at: https://projects.nilu.no//ccc/manual/index.html (last access: 6th January 2023), 2014.

NILU: EMEP data quality flags, Norwegian Institute for Air Research, available at: https://projects.nilu.no/ccc/flags/ (last access: 6th January 2023), 2020.

Oppenheimer, C., Francis, P., and Stix, J.: Depletion rates of sulfur dioxide in tropospheric volcanic plumes, Geophys. Res. Lett., 25, 2671–2674, doi:10.1029/98GL01988, 1998.

Pardini, F., Burton, M., Vitturi, M. de'Michieli, Corradini, S., Salerno, G., Merucci, L., and Di Grazia, G.: Retrieval and intercomparison of volcanic SO_2 injection height and eruption time from satellite maps and ground-based observations, J. Volcanol. Geotherm. Res. 331, 79–91, doi:10.1016/j.jvolgeores.2016.12.008, 2017.

Pattantyus, A. K., Businger, S., Howell, S. G.: Review of sulfur dioxide to sulfate aerosol chemistry at Kīlauea Volcano, Hawai'I, Atmos. Environ., 185, 262–271, doi:10.1016/j.atmosenv.2018.04.055, 2018.

Pedersen, G. B. M., Höskuldsson, A., Dürig, T., Thordarson, T., Jonsdottir, I., Riishuus, M. S., Óskarsson, B. V., Dumonta, S., Magnusson, E., Gudmundsson, M. T., Sigmundsson, F., Drouin, V. J. P. B., Gallagher, C., Askew, R., Gudnason, J., Moreland, W. M., Nikkola, P., Reynolds, H. I., and Schmith, J.: Lava field evolution and emplacement dynamics of the 2014–2015 basaltic fissure eruption at Holuhraun, Iceland, J. Volcanol. Geotherm. Res., 340, 155– 169, doi:10.1016/j.jvolgeores.2017.02.027, 2017.

Formatted: Subscript

Formatted: Subscript

Pfeffer, M., Bergsson, B., Barsotti, S., Stefánsdóttir, G., Galle, B., Arellano, S., Conde, V., Donovan, A., Ilyinskaya, E., Burton, M., Aiuppa, A., Whitty, R., Simmons, I., Arason, Þ., Jónasdóttir, E., Keller, N., Yeo, R., Arngrímsson, H., Jóhannsson, Þ., Butwin, M., Askew, R., Dumont, S., Löwis, S. von, Ingvarsson, Þ., La Spina, A., Thomas, H., Prata, F., Grassa, F., Giudice, G., Stefánsson, A., Marzano, F., Montopoli, M., and Mereu, L.: Ground-Based Measurements of the 2014–2015 Holuhraun Volcanic Cloud (Iceland), Geosciences, 8, 29, doi:10.3390/geosciences8010029, 2018.

Räty, M., Sogacheva, L., Keskinen, H.-M., Kerminen, V.-M., Nieminen, T., Petäjä, T., Ezhova, E., and Kulmala, M.: Dynamics of aerosol, humidity, and clouds in air masses travelling over Fennoscandian boreal forests, Atmos. Chem. Phys., 23, 3779–3798, doi:10.5194/acp-23-3779-2023, 2023.

Rayner, N. A., Parker, D. E., Horton, E. B., Folland, C. K., Alexander, L. V., Rowell, D. P., Kent, E. C., and Kaplan, A.: Global analyses of sea surface temperature, sea ice, and night marine air temperature since the late nineteenth century, J. Geophys. Res., 108, 4407, D14, doi:10.1029/2002JD002670, 2003.

Schmidt, A., Leadbetter, S., Theys, N., Carboni, E., Witham, C. S., Stevenson, J. A., Birch, C. E., Thordarson, T., Turnock, S., Barsotti, S., Delaney, L., Feng, W., Grainger, R. G., Hort, M. C., Höskuldsson, Á, Ialongo, I., Ilyinskaya, E., Jóhannsson, T., Kenny, P., Mather, T. A., Richards, N. A. D., and Shepherd, J.: Satellite detection, long-range transport, and air quality impacts of volcanic sulfur dioxide from the 2014–2015 flood lava eruption at Bárðarbunga (Iceland), J. Geophys. Res. Atmos., 120, 9739– 9757, doi:10.1002/2015JD023638, 2015.

Schulz, M., Textor, C., Kinne, S., Balkanski, Y., Bauer, S., Berntsen, T., Berglen, T., Boucher, O., Dentener, F., Guibert, S. and Isaksen, I. S. A., Iversen, T., Koch, D., Kirkevåg, A., Liu, X., Montanaro, V., Myhre, G., Penner, J. E., Pitari, G., Reddy, S., Seland, Ø., Stier, P., and Takemura, T.: Radiative forcing by aerosols as derived from the AeroCom present-day and pre-industrial simulations, Atmos. Chem. Phys., 6, 5225–5246, doi:10.5194/acp-6-5225-2006, 2006.

Sellar, A. A., Jones, C. G., Mulcahy, J. P., Tang, Y., Yool, A., Wiltshire, A., O'Connor, F. M., Stringer, M., Hill, R., Palmieri, J., Woodward, S., de Mora, L., Kuhlbrodt, T., Rumbold, S. T., Kelley, D. I., Ellis, R., Johnson, C. E., Walton, J., Abraham, N. L., Andrews, M. B., Andrews, T., Archibald, A. T., Berthou, S., Burke, E., Blockley, E., Carslaw, K., Dalvi, M., Edwards, J., Folberth, G. A., Gedney, N., Griffiths, P. T., Harper, A. B., Hendry, M. A., Hewitt, A. J., Johnson, B., Jones, A., Jones, C. D., Keeble, J., Liddicoat, S., Morgenstern, O., Parker, R. J., Predoi, V., Robertson, E., Siahaan, A., Smith, R. S., Swaminathan, R., Woodhouse, M. T., Zeng, G., Zerroukat, M.: UKESM1: Description and evaluation of the U.K. Earth System Model, J. Adv. Model. Earth Syst., 11, 4513– 4558, doi:10.1029/2019MS001739, 2019.

Sigmundsson, F., Hooper, A., Hreinsdottir, S., Vogfjord, K. S., Ofeigsson, B. G., Heimisson, E. R., Dumont, S., Parks, M., Spaans, K., Gudmundsson, G. B., Drouin, V., Arnadottir, T., Jonsdottir, K., Gudmundsson, M. T., Hognadottir, T., Fridriksdottir, H. M., Hensch, M., Einarsson, P., Magnusson, E., Samsonov, S., Brandsdottir, B., White, R. S., Agustsdottir, T., Greenfield, T., Green, R. G., Hjartardottir, A. R., Pedersen, R., Bennett, R. A., Geirsson, H., La Femina, P. C., Bjornsson, H., Palsson, F., Sturkell, E., Bean, C. J., Mollhoff, M., Braiden, A. K., and Eibl, E. P. S.: Segmented lateral dyke growth in a rifting event at Bárðarbunga volcanic system, Iceland, Nature, 517(7533), 191–195, doi:10.1038/nature14111, 2015.

Søvde, O. A., Prather, M. J., Isaksen, I. S. A., Berntsen, T. K., Stordal, F., Zhu, X., Holmes, C. D., and Hsu, J.: The chemical transport model Oslo CTM3, Geosci. Model Dev., 5, 1441–1469, doi:10.5194/gmd-5-1441-2012, 2012.

Steensen, B. M., Schulz, M., Theys, N., and Fagerli, H.: A model study of the pollution effects of the first 3 months of the Holuhraun volcanic fissure: comparison with observations and air pollution effects, Atmos. Chem. Phys., 16, 9745–9760, doi:10.5194/acp-16-9745-2016, 2016.

Stein, A. F., Draxler, R. R., Rolph, G. D., Stunder, B. J. B., Cohen, M. D., and Ngan, F.: NOAA's HYSPLIT atmospheric transport and dispersion modeling system, Bull. Am. Meteorol. Soc., 96, 2059–2077, doi:10.1175/BAMS-D-14-00110.1, 2015.

Stevens, B., Giorgetta, M., Esch, M., Mauritsen, T., Crueger, T., Rast, S., Salzmann, M., Schmidt, H., Bader, J., Block, K., Brokopf, R., Fast, I., Kinne, S., Kornblueh, L., Lohmann, U., Pincus, R., Reichler, T., and Roeckner, E.: Atmospheric component of the MPI-M Earth System Model: ECHAM6, J. Adv. Model. Earth Sy., 5, 146–172, doi:10.1002/jame.20015, 2013.

Stevenson, D., Johnson, C., Collins, W., and Derwent, R.: The tropospheric sulphur cycle and the role of volcanic SO_2, Geol. Soc. Spec. Publ., 213, 295–305, 2003.

Stewart, C., Damby, D. E., Horwell, C. J., Elias, T., Ilyinskaya, E., Tomašek, I., Longo, B. M., Schmidt, A., Carlsen, H. K., Mason, E., Baxter, P. J., Cronin, S., and Witham, C.: Volcanic air pollution and human health: recent advances and future directions, Bull. Volcanol., 84, 11, doi:10.1007/s00445-021-01513-9, 2022.

Stohl, A.: Computation, accuracy and applications of trajectories—A review and bibliography, Atmos. Environ., 32, 947-966, 1998.

Takemura, T., Okamoto, H., Maruyama, Y., Numaguti, A., Higurashi, A., and Nakajima, T.: Global three-dimensional simulation of aerosol optical thickness distribution of various origins, J. Geophys. Res., 105, 17853–17873, doi:10.1029/2000JD900265, 2000.

Takemura, T., Nozawa, T., Emori, S., Nakajima, T. Y., and Nakajima, T.: Simulation of climate response to aerosol direct and indirect effects with aerosol transport-radiation model, J. Geophys. Res., 110, D02202, doi:10.1029/2004JD005029, 2005.

Takemura, T., Egashira, M., Matsuzawa, K., Ichijo, H., O'ishi, R., and Abe-Ouchi, A.: A simulation of the global distribution and radiative forcing of soil dust aerosols at the Last Glacial Maximum, Atmos. Chem. Phys., 9, 3061–3073, doi:10.5194/acp-9-3061-2009, 2009.

Tatebe, H., Ogura, T., Nitta, T., Komuro, Y., Ogochi, K., Takemura, T., Sudo, K., Sekiguchi, M., Abe, M., Saito, F., Chikira, M., Watanabe, S., Mori, M., Hirota, N., Kawatani, Y., Mochizuki, T., Yoshimura, K., Takata, K., O'ishi, R., Yamazaki, D., Suzuki, T., Kurogi, M., Kataoka, T., Watanabe, M., and Kimoto, M.: Description and basic evaluation of simulated mean state, internal variability, and climate sensitivity in MIROC6, Geosci. Model Dev., 12, 2727–2765, doi:10.5194/gmd-12-2727-2019, 2019.

Tegen, I., Neubauer, D., Ferrachat, S., Siegenthaler-Le Drian, C., Bey, I., Schutgens, N., Stier, P., Watson-Parris, D., Stanelle, T., Schmidt, H., Rast, S., Kokkola, H., Schultz, M., Schroeder, S., Daskalakis, N., Barthel, S., Heinold, B., and Lohmann, U.: The global aerosol–climate model ECHAM6.3–HAM2.3 – Part 1: Aerosol evaluation, Geosci. Model Dev., 12, 1643–1677, doi:10.5194/gmd-12-1643-2019, 2019.

Theys, N., De Smedt, I., Yu, H., Danckaert, T., van Gent, J., Hörmann, C., Wagner, T., Hedelt, P., Bauer, H., Romahn, F., Pedergnana, M., Loyola, D., and Van Roozendael, M.: Sulfur dioxide retrievals from TROPOMI onboard Sentinel-5 Precursor: algorithm theoretical basis, Atmos. Meas. Tech., 10, 119–153, doi:10.5194/amt-10-119-2017, 2017.

Theys, N., Campion, R., Clarisse, L., Brenot, H., van Gent, J., Dils, B., Corradini, S., Merucci, L., Coheur, P.-F., Van Roozendael, M., Hurtmans, D., Clerbaux, C., Tait, S., and Ferrucci, F.: Volcanic SO_2 fluxes derived from satellite data: a survey using OMI, GOME-2, IASI and MODIS, Atmos. Chem. Phys., 13, 5945–5968, doi:10.5194/acp-13-5945-2013, 2013.

Formatted: Subscript

Formatted: Subscript

Thordarson, T., and Hartley M.: Atmospheric sulfur loading by the ongoing Nornahraun eruption, North Iceland, Geophys. Res., Abstracts, 17(EGU2015-10708), 2015.

Toll, V., Christensen, M., Gassó, S., and Bellouin, N.: Volcano and ship tracks indicate excessive aerosol-induced cloud water increases in a climate model, Geophys. Res. Lett., 44, 492–412,500, doi: doi.org/10.1002/2017GL075280, 2017.

Tørseth, K., Aas, W., Breivik, K., Fjæraa, A. M., Fiebig, M., Hjellbrekke, A. G., Lund Myhre, C., Solberg, S., and Yttri, K. E.: Introduction to the European Monitoring and Evaluation Programme (EMEP) and observed atmospheric composition change during 1972–2009, Atmos. Chem. Phys., 12, 5447–5481, doi:10.5194/acp-12-5447-2012, 2012.

Twigg, M. M., Ilyinskaya, E., Beccaceci, S., Green, D. C., Jones, M. R., Langford, B., Leeson, S. R., Lingard, J. J. N., Pereira, G. M., Carter, H., Poskitt, J., Richter, A., Ritchie, S., Simmons, I., Smith, R. I., Tang, Y. S., Van Dijk, N., Vincent, K., Nemitz, E., Vieno, M., and Braban, C. F.: Impacts of the 2014–2015 Holuhraun eruption on the UK atmosphere, Atmos. Chem. Phys., 16, 11415–11431, doi:10.5194/acp-16-11415-2016, 2016.

Väänänen, R., Kyrö, E.-M., Nieminen, T., Kivekäs, N., Junninen, H., Virkkula, A., Dal Maso, M., Lihavainen, H., Viisanen, Y., Svenningsson, B., Holst, T., Arneth, A., Aalto, P. P., Kulmala, M., and Kerminen, V.-M.: Analysis of particle size distribution changes between three measurement sites in northern Scandinavia, Atmos. Chem. Phys., 13, 11887–11903, doi:10.5194/acp-13-11887-2013, 2013.

~~Vignati, E., Wilson, J., and Stier, P.: M7: An efficient size-resolved aerosol microphysics module for large-scale aerosol transport models, J. Geophys. Res., 109, D22202, doi:10.1029/2003JD004485, 2004.~~

Walker, J. C., Dudhia, A., and Carboni, E.: An effective method for the detection of trace species demonstrated using the MetOp Infrared Atmospheric Sounding Interferometer, Atmos. Meas. Tech., 4, 1567–1580, doi:10.5194/amt-4-1567-2011, 2011.

Walker, J. C., Carboni, E., Dudhia, A., and Grainger, R. G.: Improved detection of sulphur dioxide in volcanic plumes using satellite-based hyperspectral infrared measurements: Application to the Eyjafjallajökull 2010 eruption, J. Geophys. Res., 117, D00U16, doi:10.1029/2011JD016810, 2012.

Walters, D., Baran, A. J., Boutle, I., Brooks, M., Earnshaw, P., Edwards, J., Furtado, K., Hill, P., Lock, A., Manners, J., Morcrette, C., Mulcahy, J., Sanchez, C., Smith, C., Stratton, R., Tennant, W., Tomassini, L., Van Weverberg, K., Vosper, S., Willett, M., Browse, J., Bushell, A., Carslaw, K., Dalvi, M., Essery, R., Gedney, N., Hardiman, S., Johnson, B., Johnson, C., Jones, A., Jones, C., Mann, G., Milton, S., Rumbold, H., Sellar, A., Ujiie, M., Whitall, M., Williams, K., and Zerroukat, M.: The Met Office Unified Model Global Atmosphere 7.0/7.1 and JULES Global Land 7.0 configurations, Geosci. Model Dev., 12, 1909–1963, doi:10.5194/gmd-12-1909-2019, 2019.

Wells, A. F., Jones, A., Osborne, M., Damany-Pearce, L., Partridge, D. G., and Haywood, J. M.: Including ash in UKESM1 model simulations of the Raikoke volcanic eruption reveals improved agreement with observations, Atmos. Chem. Phys., 23, 3985–4007, doi:10.5194/acp-23-3985-2023, 2023. ~~Wells, A. F., Jones, A., Osborne, M., Damany-Pearce, L., Partridge, D. G., and Haywood, J. M.: Including ash in UKESM1 model simulations of the Raikoke volcanic eruption reveal improved agreement with observations, EGUsphere [preprint], doi:10.5194/egusphere-2022-1060.~~

~~Williams, K. D., Copsey, D., Blockley, E. W., Bodas-Salcedo, A., Calvert, D., Comer, R., Davis, P., Graham, T., Hewitt, H. T., Hill, R., Hyder, P., Ineson, S., Johns, T. C., Keen, A. B., Lee, R. W., Megann, A., Milton, S. F., Rae, J. G. L., Roberts, M. J., Scaife, A. A., Schiemann, R., Storkey, D., Thorpe, L., Watterson, I. G., Walters, D. N., West, A., Wood, R. A., Woollings, T., Xavier, P. K.: The Met Office Global Coupled model 3.0 and 3.1 (GC3.0 and GC3.1) configurations, J. Adv. Model. Earth Syst., 10, 357–380, doi:10.1002/2017MS001115, 2017.~~

Witham, C., Kristiansen, N., Beckett, F., and Marenco, F.: Towards a global sulphur dioxide forecast capability for aviation, Forecasting Research, Tech. Rep. No. 648, Met Office, 2021.